STARS

2018

Hole Selective Tunneling Oxide Applications with Insight into Sophisticated Characterization Techniques

Nizamettin Kortan Ogutman
University of Central Florida

Showcase of Text, Archives, Research & Scholarship

HOLE SELECTIVE TUNNELING OXIDE APPLICATIONS WITH INSIGHT INTO SOPHISTICATED CHARACTERIZATION TECHNIQUES

by

N. KORTAN ÖĞÜTMAN

B.S in Electrical and Electronics Engineering, Bahçeşehir University, 2012.
M.S. in Optics, University of Central Florida, 2013.

A dissertation submitted in partial fulfillment of the requirements
for the degree of Doctor of Philosophy
in the Department of Electrical and Computer Engineering
in the College of Engineering and Computer Science
at the University of Central Florida
Orlando, Florida

Spring Term
2018

Major Professor: Winston V. Schoenfeld

ABSTRACT

Tunneling metal oxide layers combined with industrially applicable novel cleaning methods can boost the current efficiency limit, which corresponds to approximately %22 in production, of crystalline silicon (c-Si) solar cells. Within the scope of this dissertation, extremely thin tunneling layers (1-3nm) of aluminum oxide is studied in conjunction with the development of wet cleaning procedures that are feasible in production lines currently exist today. These tunneling stacks are deployed to serve as exceptional surface passivation layers due to the inherent built-in charge provided by aluminum oxide. This capability is further strengthened by the introduction of extremely well controlled wet chemical oxide which not only saturates the dangling bonds at the interface but also enables conformal growth of the aforementioned tunneling oxide layers. Therefore, the interplay between aluminum oxide thickness, which effects the passivation quality tremendously, and carrier extraction capability (contact resistance) is also taken into account by the choice of ultimate boron doping profile and the optimization of the cleaning procedure. The resulting hole collecting surface passivation stack applied on doped surfaces provided record values of recombination current densities, with highly applicable contact resistivity values, enabling one-dimensional carrier transport. This dissertation is also concerned with spatially resolved characterization methods of such industrial c-Si solar cells given the importance of defects that can exist in these large area devices. Analytical image processing algorithms pertaining to biased-photoluminescence (PL) measurements are conducted to portray 2D maps of physical significant devices parameters such as dark saturation current density and efficiency. Finally, Fourier analysis is added into the analysis of raw PL images to pick up only the defected regions of the cells.

Dedicated to my family

ACKNOWLEDGMENTS

TABLE OF CONTENTS

LIST OF FIGURES

LIST OF TABLES

CHAPTER 1 – INTRODUCTION

1.1 Impact of Photovoltaics

With the new solar age starting in the light of promises made at the biggest scale at the Climate Summit in Paris on December 2015 [1], many major economies in the world have come to a consensus to take action on the global warming effects so that it does not reach values about 2℃. Even though the path to achieve this effort may seem clear in terms of adopting more renewables instead of carbon dioxide emitting alternatives and uncompromising nuclear, the recent improvements in cost of solar had to be realized so that the most promising renewable energy source could compete with what is already available in retail.

The unprecedented demand for energy today presents itself as one of the biggest challenges of the future to be tackled. In the world we occupy, more than %50 percent of the energy need has to be supplied by means of burning fossil fuels. And since the beginning of early commercial oil drilling in 1850s, mankind has exhausted more than 135 billion tons of crude oil to satisfy the needs such as powering our cars (%44), to warm up our houses, and even to lay down asphalt (%3) [2, 3]. Most importantly, even "some" may disagree, this consumption of fossil fuels has resulted in swelling of greenhouse gasses in the atmosphere, and is a major cause of global warming as we face it today. Even in the presence of this tremendous energy demand, today, there is still more than 1.2 billion people who do not have access to electricity. Interestingly enough, the majority of these people reside in developing countries with ubiquitous access to solar irradiance. This developing countries as classified by United Nations and International Monetary Fund, are situated within the region spanning 35 degrees of the equator [4]. This territory is known as the "sunbelt" providing highest possible solar resources, implying that application of solar panel will harvest

more energy during the day. One significant drive force for the adaptation of solar energy in these parts of the world is that in contrast to well-developed countries with fossil fuel infrastructure, there is the absence of high power transmission lines, which can be compensated by the use of batteries. As comparable to other renewable energy sources such as wind, solar is also an intermittent power supply which distinguishes itself from the others by being capable of satisfying the energy demand during peak hours. So, the enhances in battery technology serve for the better in not only dealing with the problem of intermittency, but also making the common grid structures dispensable. In countries where the solar deployment is prevalent, regular energy sources (e.g., nuclear, gas, and coal) can be structured to be run on idle, while being ready to be ramped up in case sunshine disappears. This circumstance is another instant where the use of batteries is emphasized as the common grid infrastructure can only benefit %10 from the solar irradiance without proper energy storage. Therefore, solar energy presents itself, in addition to satisfying the need for energy especially during the peak hours of the day, as the sole candidate to enable a better life standard in less developed countries. It is the very absence of these aforementioned transmission lines which makes the implementation of solar energy in developing countries appealing. This stems from the fact that even though solar energy may require significant upfront payment, which has been the biggest bottleneck for deployment in developed countries, the underdeveloped counterparts acquire their energy needs from costly options like fuel oil plants which costs around 0.40$ per kWh [4]. This situation occurs due to the absence of competition with cheap alternatives such as gas and coal. Therefore, solar energy, coming only at prices around 0.10$ per kWh, is a serious contender to contribute to the fight against the climate resilience as the energy growth rate is projected to hit %71 by 2040 in developing countries [4].

As claimed by the World Meteorological Organization (WMO), there is a 0.83℃ increase in temperature on Earth's atmosphere, as compared to pre-industrial references, due to global warming. The intergovernmental panel on climate change (IPCC) forecasts that a temperature changes between 2.6-4.8℃ on earth's crust by 2100, which corresponds to a 0.26-0.55 meters of sea-level rise [4]. To be able to grasp the impact of such a catastrophe, researchers have come up with a metric named Climate Change Vulnerability Index to portray this in the global sense.

Rank	City	Category
1	Dhaka	Extreme
2	Manila	Extreme
3	Bangkok	Extreme
4	Yangon	Extreme
5	Djakarta	Extreme
6	Ho Chi Minh	Extreme
7	Kolkata	Extreme
8	Mumbai	High
9	Chennai	High
10	Lagos	High
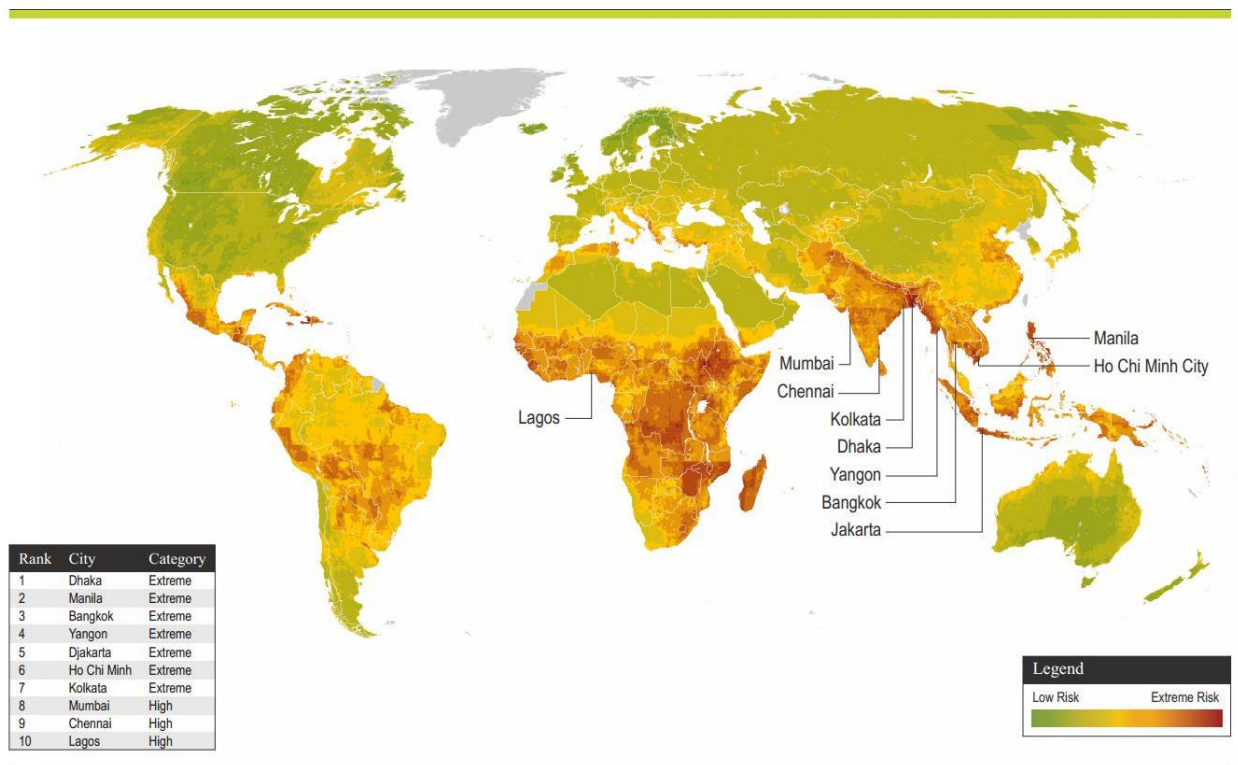
Figure 1 : Verisk Maplecroft's 2017 Climate Change Vulnerability Index.

As it is observed, developing countries are devastated much more significantly than the rest of the world as they are more vulnerable to climate change adaptation due to number of reasons (e.g., poverty, densely populated, low resilience to flood and drought).

1.2 Economies of Scale

No matter what the benefits of non-hydro renewables are, the switch over to these alternative sources can only be realized if the market penetration is deemed meaningful. Since the very initial showcase of PV devices as a mainstream energy source in 1973, there has a been monumental decrease in price from 500$/Watt to less than 1$/Watt (Monetary values in 1973 are adjusted in accordance with 2015 US $ equivalent). With the record deployment rate in 2016, 76.6 GW of solar energy is installed into the grid making it %50 growth rate as compared to 51.2 GW the year before. This creates more than a US$100 billion industry promoting solar as one of the largest, if not the largest, optoelectronics market in world with flat-panel displays and solid-stated lighting [5].
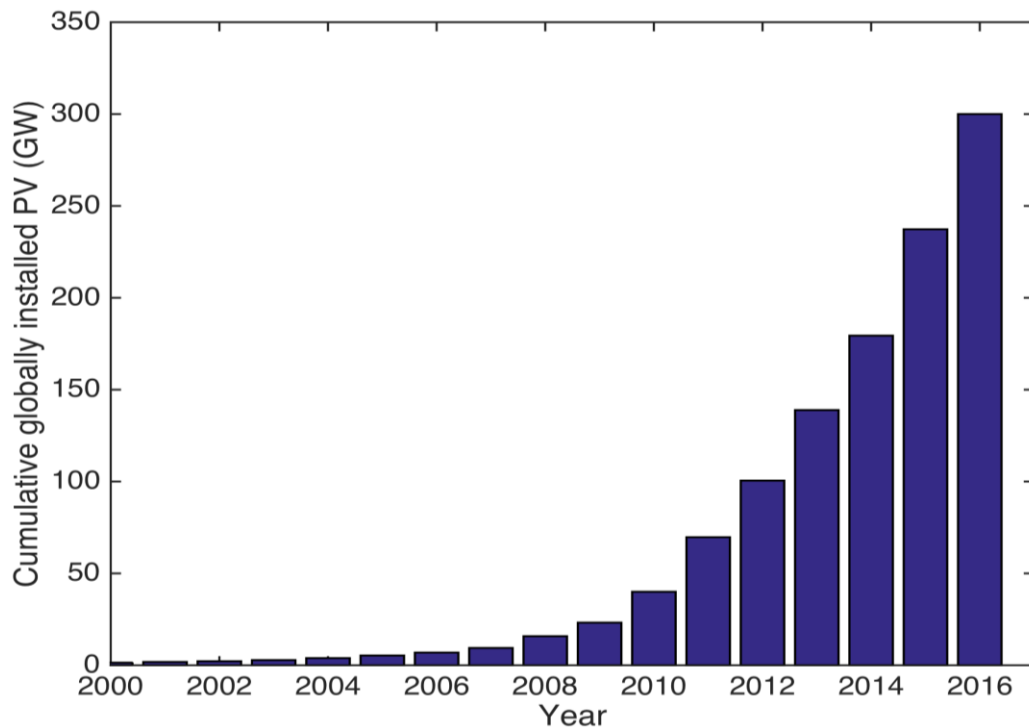
Figure 2 : Evolution of globally installed solar energy between 2000-2016.

The competitiveness of solar is often judged by what is called "grid parity", which denotes that the projected cost of electricity provided by the photovoltaic system either matches or is cheaper than the price of electricity that is already available. The major drivers for grid parity to take place is (1) innovation in photovoltaic technologies, (2) simplification/optimization of the manufacturing processes, (3) increased deployment, and (4) the use of lower-cost materials. One major innovation that took place in the late 1970s is the introduction of the back-surface field (BSF) which reduced the recombination losses drastically, and is still the most dominant PV technology today. Another key improvement that enabled accelerated adoption of this technology was the introduction of silicon nitride (SiN_x) films, deposited by plasma-enhanced chemical vapor deposition (PECVD) that not only provided really high passivation values on phosphorous diffused surfaces but also served as antireflective coatings (ARC). These two major advances combined with a number of others (e.g., screen-printed contacts, mono-texturing) allowed ubiquitous adoption of crystalline silicon photovoltaics technology.

Mankind, as of today, consumes more than 10^{18} Joules of energy in a day, which corresponds to 12 TW approximately. And given the total deployment capacity of solar power (300MW), a total of %0.0025 of world's energy need can be supplied by this alternative source. However, this only portrays the global pictures, in certain countries this adaptation is taking place in a much more significantly manner. To provide a sense of scale that solar power represents as a future energy replacement prospect, an hour of sunlight hitting earth's surface can meet humanity's energy demand for a year. To depict this picture in numbers, available solar resource on earth's crust is 3.6×10^4 TW_{ave} compared to 50 TW_{ave} (Human energy usage mid-to late century). To satisfy this need by a source like nuclear energy, 3000 times the daily output of Palo Verde nuclear station would be required [2].

The metric that highlights the practicality of solar energy usage is what is called Levelized-Cost of Electricity (LCOE), which is defined as the lifetime costs of a system divided by energy produced. This allows direct comparisons of different competing technologies of comparable lifetimes, and capital costs. Given the maturity of solar industry, the efficiency values can be overseen and guaranteed for an extended period of time (~20 years), which makes the LCOE calculation meaningful.
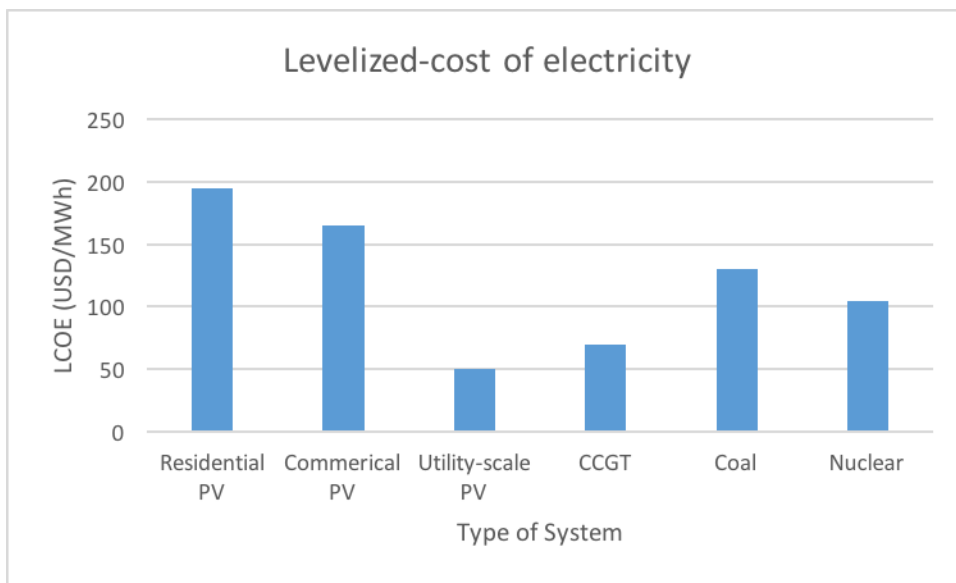
Figure 3 Levelized cost-of solar electricity as compared with other power sources.

What is depicted in Fig.3. is the LCOE associated, as calculated by US investment bank Lazard Capital, with utility-scale solar energy, as of 2016, is cheaper than coal, nuclear power, and even combined cycle gas turbines (CCGT) [1].
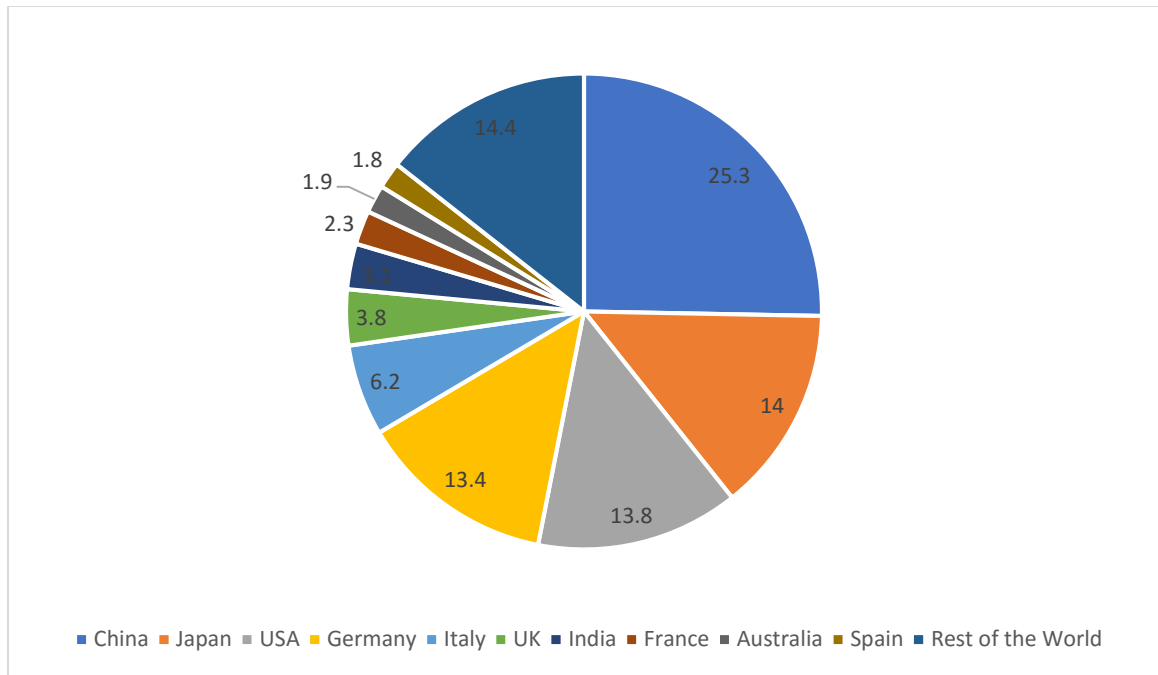
Figure 4 Top 10 Solar PV Markets installed Shares By End of 2016.

What Fig.4. illustrates is the impact of subsidies on solar deployment, which mainly dominated by Chinese government, thus the more than %25 share. The other important take-away is that even though solar may provide, as of 2016, minor portion of world's energy need, it is impact on certain economies cannot be overlooked. For instance, Italy can obtain %7.5 of its nation's electricity demand from photovoltaic capacity (19.28GW).

What appeals a solar system, in terms of economics, is its payback time, which signifies the duration it takes for electricity produced by the photovoltaic system to cover the initial cost of installation. One factor that complements the tremendous reduction in payback time is the material usage per Watt peak (W_p). 12 years ago, 16 grams of silicon had to be used per W_p, and today, owing to increased efficiencies and thinner wafers, 6 g/W_p is feasible. All of the aforementioned advances makes it possible for certain sunny locations in the world to have quite fast payback

times. For example, a photovoltaic array in Sicily (Southern Italy) which features multi-crystalline silicon solar cells possesses an energy payback time of approximately one year. This implies that this system, in its 20-year lifespan, will create twenty times the energy required to install it. Therefore, technological advances and economies of scale enable a drastic cost reduction of %90 in rooftop photovoltaic systems over a period of 25 years, and figure below illustrates a similar trend between 2010 and 2015.
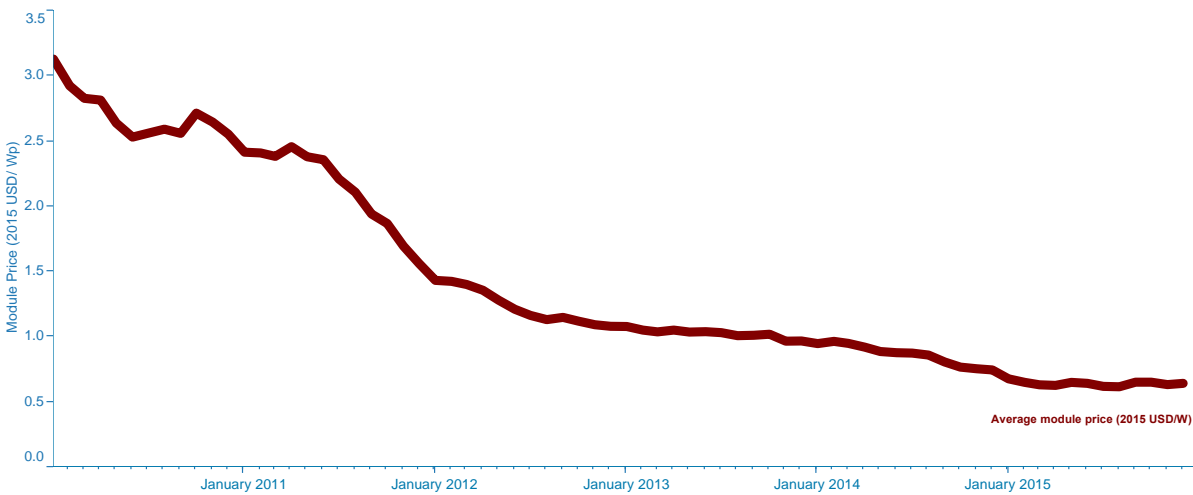
Figure 5 Cost-trend associated with crystalline silicon modules between 2010-2015 (Source: International Renewable Energy Agency).

CHAPTER 2 - PHYSICS OF CRYSTALLINE SILICON PHOTOVOLTAIC CELLS

2.1 Why Silicon?

The reason why silicon photovoltaic devices constitute more than %90 of the total PV devices made today will be the subject of this part of my dissertation. The chief among those reasons is the fact that silicon is the second most abundant material on Earth's crust right after the most abundant one, oxygen [6]. Silicon being the most abundant semiconductor plays a very crucial role in terms of it scalability as a product, which started its lifetime in integrated circuit industry. Though being purified around the same time as silicon, germanium possesses a smaller band-gap which introduces more thermally excited carriers in the conduction band. Furthermore, one other inherent property of Si is that at room temperature, as it interacts with air, it forms a very strong oxide at the surface (thickness ~1nm) within hours of exposure [7]. The driving mechanism for this native oxide growth is the presence of oxygen and water (moisture). This avoids many concerns with degradation as this may not be the case with other organic photovoltaic devices. Another factor that contributes to the dominance is the bandgap of silicon. This among many possible other reasons, comes into play in two flavors. First, it is quite beneficial to have high refractive index (n=3.55 at $\lambda = 1050nm$) so that due to the high index gradient, larger back surface reflection coefficient is obtained. There is usually a dielectric passivation layer at the back surfaces of these devices complementing this feature. Even though silicon can be thought of as a "poor" absorber, being an indirect bandgap material, the high refractive index can be exploited for light trapping purposes. This indirect bandgap behavior leads to a low light absorption of coefficient ($<10^4 cm^{-1}$) for photons that have energy lower than 3.4eV.
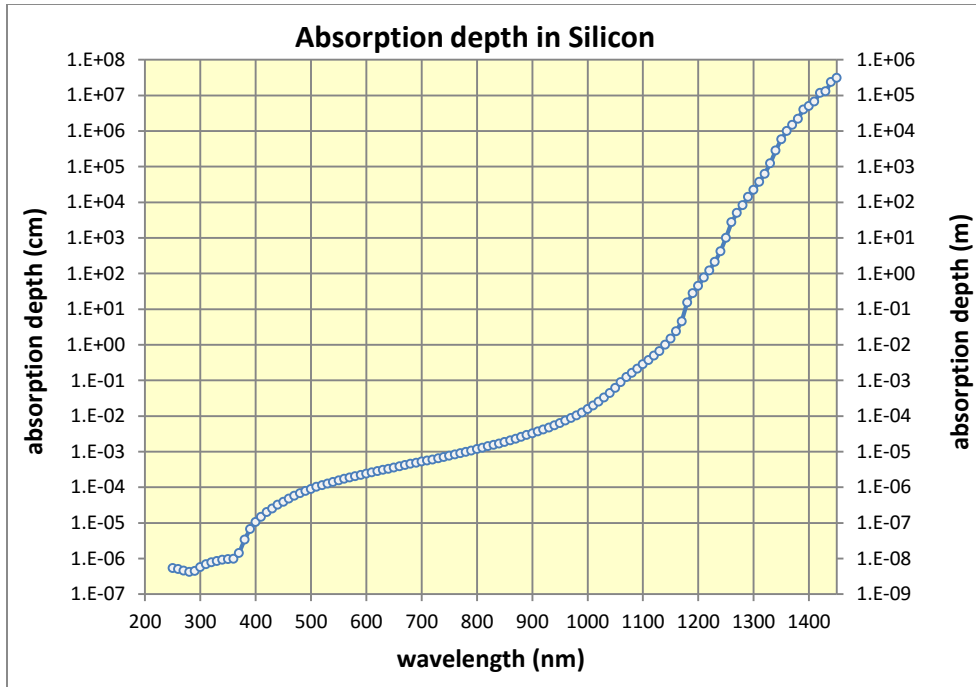
Figure 6 Absorption depth in silicon at room temperature (300K) [8].

As illustrated in Figure 6, the absorption behavior of silicon requires thickness values between $100-200\mu m$ so that enough light is absorbed. This thickness also comes into play due to silicon being a brittle substance at room temperature, creating mechanical issues of handling. Given these challenges, exceptional light absorption can still be enabled in silicon. Yablonovitch [9]came up with an upper limit for this trapping property which scales with the real part of the refractive index, the famous $4n^2$. This implies that for the case of silicon, one could possibly force the captured photon inside the device to travel as much as 50 times before it is absorbed. The second, which probably is one of mature nature's miracles, is that silicon sits very close to the ideal single-junction band-gap energy (~1.1eV at T=300K) that provides the highest possible conversion efficiency. This upper theoretical limit of efficiency is determined under the principles of detailed-balance, which dictates that in thermal equilibrium all the microscopic actions are

counterbalanced by the corresponding inverse processes. In the context of solar cells, this is perceived as all the generation processes must be neutralized (for the sake of zero excess carriers) by radiative recombination. This principle, to foresee the highest possible conversion efficiency value, neglects the non-radiative recombination processes, which in turn entails that a perfect solar cell acts also as an ideal light emitting diode (LED)[10], [11]. This is further illustrated by the below equation.

$$EQE_{LED} = \frac{R_{rad}}{R_{rad}+R_{non-rad}} \tag{1}$$

, where EQE_{LED}, R_{rad}, $R_{non-rad}$, represents external quantum efficiency of an LED, radiative recombination rate, and non-radiative recombination rate, respectively. As can be deduced, in the absence of non-radiative recombination, external quantum efficiency of the LED device turns out to be unity. In the idealized case of Schokley-Queisser limit, an ultimate efficiency is determined by the bandgap (E_g) and the temperature of the solar cell, wherein all the photons having energies higher than E_g is absorbed and collected at the junction perfectly. This view can also be perceived as a solar cell being a simple energy converting engine that is capable of creating electrical work following the heat absorption coming from the sun. In the broader sense, when one considers the more fundamental limits of physics, namely the thermodynamics limit, the maximum attainable efficiency turns out to be %95 for any solar device operating at T=300K. This absolute possible limit depends on the ratio of source (sun) temperature (T=6000K) to the surrounding heat sink, in this case a solar cell operating at room temperature. Of course, there is further deductions

from this uttermost maximum, the chief among which occurs via lattice vibrations, phonons. This phenomenon takes place due to the fact that when a photon $(h\nu \geq E_g)$ impinges on a semiconductor, an electron-hole pair will be generated given that absorption occurs. Moreover, the resulting photo-excited electron, having energy in excess of the bandgap, is considered to be a "hot" carrier before any scattering events happen in the presence of lattice phonons. Following the numerous scattering action, this aforementioned hot electron will donate its excess energy to the lattice, in the form of heat, as it relaxes down to the fundamental conduction band. This relaxation loss mechanism constitutes 47.4% of the total losses from the thermodynamics limit [12]. This concept by the name of hot-carrier solar cell (HCSC), after being proposed in 1982 by Ross and Nozik [13]. There are number of reasons that prohibited the practical adaptation of such structures, the most important one being the energy selective contacts. In the more practical side of things, Shockley-Queisser limit is concerned with a single p-n junction silicon device, with a given bandgap (1.12eV), yielded an efficiency limit of approximately %29.5 under global air mass 1.5 (AM 1.5G) solar spectrum. As can be seen, this is a more "realistic" limit, as it only depends on the bandgap and the spectrum shining on the device. The major insight that enabled this ultimate efficiency limit calculation is that there has be a match between the rate of emission of photons and the rate of absorbed photons so that under steady-state circumstances electron concentration inside the material do not vary in time. Under illumination, the incident flux of photons impinging on the solar cell in air is given by the following equation,

$$f(E, \Delta\eta) = \frac{2\pi}{h^3 c^2} \frac{E^2}{e^{(E-\Delta\eta)/(k_B \cdot T)} - 1} \tag{2}$$

, where $E, \Delta\eta$, h, c, k_B, T represent the energy of a photon, separation of the quasi-Fermi levels, Planck's constant, speed of light, Boltzmann constant, and the ambient temperature. Equation 2 can be used to portray the ultimate possible efficiency as a function of the bandgap of the material of interest, which guides the decision of what can be a good candidate as a solar cell.
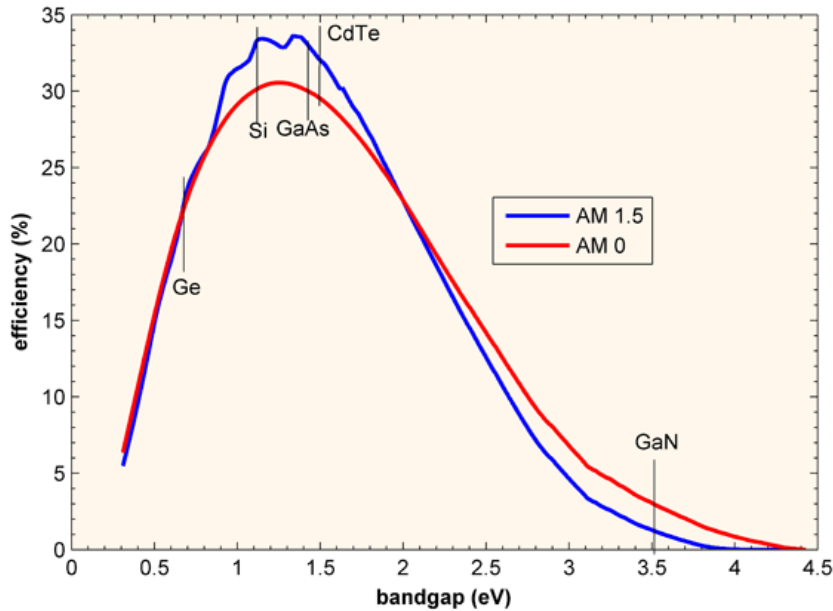
Figure 7 Theoretically possible solar cell efficiency as a function of material bandgap for one-sun illumination [14, 15].

From Figure 7, one can conclude that silicon and gallium arsenide (GaAs) are positioned very close to the ultimate efficiency peaks that are neighboring each other. This phenomenon is also put into production in real life. The Silicon solar cells already provided short-circuit current density (J_{sc}) values of $42.7 \, mA/cm^2$, in comparison to the theoretical maximum of $43.85 \, mA/cm^2$. GaAs, having a bandgap of 1.43eV, devices are made to produce a maximum short-circuit current density of $29.68 \, mA/cm^2$, not for away from the theoretical maximum of $31.76 \, mA/cm^2$ [16]. Since the maximum power output involve the voltage term, the control on recombination processes

plays a crucial role in delivering the ultimate open-circuit (V_{oc}). Furthermore, as the voltage depends exponentially on the excess carrier density, whatever is lost to recombination events will impact this variable drastically. One of the outcomes of the SQ-limit, in essence, actually relates back to a good solar cell being a good LED. This is further emphasized by how close the actual open-circuit voltage values resembles the ideal one, as shown by the relation below [10, 17].

$$\Delta V_{oc} = V_{oc,rad} - V_{oc} = -\frac{k_B \cdot T}{q} \ln(Q_{LED}) \qquad (3)$$

, where $V_{oc,rad}, V_{oc}, k_B, T$,q represent the open-circuit voltage at radiative limit, the actual voltage, Boltzmann constant, temperature and the electrical charge respectively. So, by observing how good the device is as a light emitter, one can deduce how close they are to the theoretical limit of open-circuit voltage. As will be shown later in this dissertation, light emission properties of solar cells can be exploited to reveal information about the electrical properties of these devices. An intuitive way to portray the SQ-limit which relates, in essence, to finding the ultimate bandgap energy can be done in the following way. Since as the bandgap increases, the smaller part of the spectrum will be subject to absorption by the device, there will be a short-circuit current density decrease. On the flipside, a smaller bandgap will provide access to absorption of carrier from a wider spectrum, the resulting open-circuit voltage will diminish. Therefore, this interplay between these two variables, J_{sc} and V_{oc}, that determine the output power of a solar cell, plays a significant role in determining the desired bandgap energy. Table below shows the record breaking efficiencies for the aforementioned best single junction candidates, namely silicon and gallium arsenide-based solar converters.

Table 1. Overview of current cell performance metrics with their theoretical limits[16, 18].

	$J_{sc}(mA/cm^2)$		$V_{oc}(V)$		$\eta(\%)$	
	limit	record	limit	record	limit	record
Si	43.85	42.7	761	750	29.4	26.61
GaAs	31.76	29.68	1.170	1.122	33.72	28.8

The ultimate choice, up to now, that enables the highest efficiency values that approaches SQ-limit for the case of silicon has been the heterojunction inter-digitated back-contact solar cell (HJ-IBC). This hetero structure, in contrast to homojunction architectures, provides exceptionally high passivation without sacrificing carrier extraction penalties. What this implies that even though passivation layers that have been showcased in homojunction devices, such as aluminum oxide (Al_2O_3), is capable of providing comparable saturation current densities, due to their dielectric nature, they inhibit carrier transport. This not only brings the necessity for more than 1-dimensional carrier extraction paths, but also creates local contact points where metal touches the silicon substrate directly resulting in high recombination. However, as will be shown within the flow of this dissertation, these well-known dielectric passivation stacks (Al_2O_3) can also be exploited as tunneling layers, featuring 1-dimensional carrier extraction, to be used in industrially relevant conditions. The best performing homojunction device that lacks both the back contact complexities and the local contact openings has been the tunnel oxide passivated contact (TOPcon) architecture. This device exhibits a full-area charge selective back surface, yielding a conversion efficiency of %25.3 with an open-circuit voltage of 718V [18]. To provide the best of both worlds, in terms of short-circuit current and open-circuit voltage, HJ-IBC concept has been proposed [18], wherein the placement of contacts in the back avoids the shading loss mechanisms, and the hybrid

contacts provide V_{oc} values approaching the theoretical limit. There are number of reasons why even the best laboratory cells deviate from the ultimate efficiency value, chief among which is called Shockley-Read-Hall (SRH) recombination mechanism. SRH can take place at a variety of location within a silicon device, either at the surface or in the bulk. Another significant factor, which is assumed in the derivation of SQ-limit, is that real solar cells do possess zero reflection in front and %100 Lambertian reflection in the back, thus exhibiting optical losses. The final main factor, which becomes especially critical in situations where multiple-dimensional carrier transport takes place, is the presence of resistive losses. Since this work is aimed to provide an industrially relevant alternative solution to SRH problem, different recombination mechanisms will be reviewed in detail in a separate section.

Furthermore, silicon inherently forms sp3 hybridized orbitals, implying that it is bound to 4 neighboring atoms (tetrahedral connection), which ultimately brings a tremendous advantage in term of solid solubility of impurities. This sp-hybrid chemical bonding does not permit incorporating metal impurities into a growing crystalline silicon. This occurs due to the fact that a great energy (~10eV) is required for the electron shell restructuring concerned with d-atom [19]. Therefore, silicon is capable of rejecting impurities from the solid into the melt giving rise to effective purification of the material during the growth process. This resistance towards these metal impurities enable the growth of silicon substrates with extremely high bulk lifetime values (>10ms) paving the way for high efficiency devices.

2.2 Different Recombination Mechanisms

The following sections will concern with different recombination mechanism through which a generated carrier is lost. These processes can be categorized into two flavors: unavoidable

recombination mechanisms that occur due to basic physical phenomenon (e.g. radiative recombination), and avoidable ones that take place because of imperfections, which can be engineered to be benign.

2.2.1 Radiative Recombination

Though for the case of silicon this may not be limiting recombination process owing to the indirect bandgap nature of silicon, radiative recombination can still play a significant role in other direct bandgap high efficiency solar converters such as gallium arsenide. Since spontaneous emission behavior directly relates to how good of an absorber the material really is, then one could write the total radiative recombination rate by also taking into consideration the incoming flux.

$$U_{rad}^{total} = \int \alpha(E)\varphi(E,\Delta\eta)dE \qquad (4)$$

, where $\alpha(E)$, $\varphi(E,\Delta\eta)$, represents the absorption coefficient and the incoming flux respectively. Subtracting the radiative recombination rate due to thermally excited carriers, one obtains the net radiative recombination rate as follows.

$$U_{rad} = \int \alpha(E)\varphi(E,\Delta\eta)dE - \int \alpha(E)\varphi(E,0)dE \qquad (5)$$

, which can be written simply as follows,

$$U_{rad} = B_{rad}(np - n_i^2) \qquad (6)$$

, with B_{rad} being radiative recombination coefficient which is an inherent property of the semiconductor (independent of carrier densities). To provide a sense of scale that highlights the dominance of this recombination channel, silicon radiative lifetime is in the order of nanoseconds, whereas in the case of GaAs this variable can be seconds.

2.2.2 Auger Recombination

The second, and the last, unavoidable carrier depletion mechanism in photovoltaic devices takes place due to the kinetic collision between carriers of same polarity, promoting one to a higher kinetic energy while the other recombines with a carrier that has opposite polarity. Within this process upon recombination, instead of emitting a photon, the excess energy is consumed to promote the electron to a higher energy within the band. This implies that Auger recombination will consist of an electron and two holes or a hole and two electrons. As the excited carrier releases its excess kinetic energy to reach the band edge, this energy will be dissipated as heat, thus another loss factor. This third carrier, as the transition to its initial energy state goes on, emits phonons, and as mentioned earlier with the current state of the technology these phonon energies cannot be exploited. The total Auger recombination rate, as can be deduced from the number of interacting species (e.g. electron + 2 holes) can be written in the following manner.

$$U_{Aug} = C_n(n^2p - n_op_o) + C_p(np^2 - n_op_o) \tag{7}$$

, where C_n (1.7-2.8 $x10^{-31}cm^6/s$), C_p (0.99-1.2x$10^{-31}cm^6/s$) are called Auger coefficients for electrons and holes respectively, and are independent of carrier concentrations for the case of non-interacting free particles. The most obvious way of determining these constants is to measure the effective lifetime under low-injection conditions as a function of doping concentration [20].

The impact of Auger recombination diminishes as the doping density or the injection level is decreased. This type of recombination, as expected comes into play in high-quality silicon devices. Therefore, the effective carrier lifetimes within the emitters of such devices are most often limited by Auger recombination. Lastly, Auger recombination is much more pronounced in indirect-band gap materials as the energy loss occurs via the release of phonons. Figure below depicts the aforementioned two possibilities for Auger recombination.
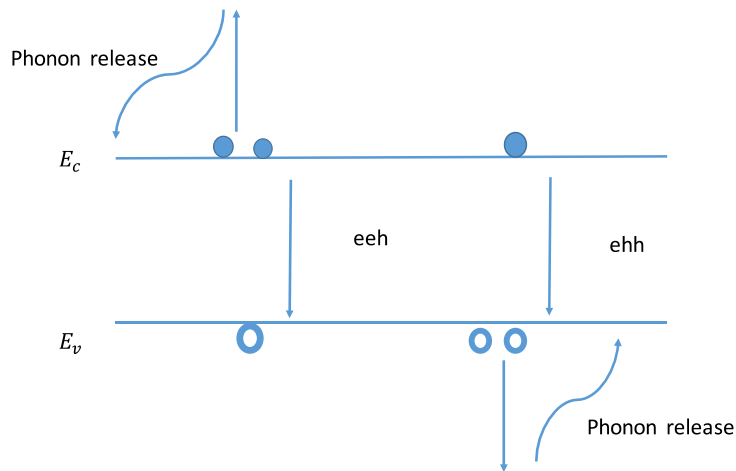
Figure 8 Auger recombination is shown for both carrier interaction pathways.

2.2.3 Shockley Read Hall Recombination (Recombination via defect states)

Shockley Read Hall (SRH) recombination constitutes the most significant portion of all carrier loss mechanisms in real photovoltaic devices that is made of indirect bandgap materials.

As will be covered here, this theory can be applied not only to bulk defects but also surface imperfections. The possibilities that can be evaluated within the scope of SRH statistics encompasses impurities (located either at bulk or at surface), dislocations, and disturbances in the symmetry of crystal lattice, which again can take place either at bulk (e.g. multi-crystalline material), or at surface (e.g. dangling bonds).

2.2.3.1 Recombination in the bulk

If the impurities arising from foreign chemical elements or the presence of lattice defects (e.g. the absence of a host atom, dislocations, an interstitial atom) exist in a semiconductor material, a significant disturbance to the periodic potential of the crystalline structure takes place. In case this potential gradient is large enough, a charged carrier can be forced to be trapped inside this potential "well". Deep trapping behavior is expected in the presence of elements from the I, II, VI, and VII columns of periodic table. Their chemical distributions (charge distribution) is significantly disparate from that of the host atom which, in silicon's case, is a column IV element, and this creates trap centers that lie deeper in the bandgap of the host material, while column III and V impurities generate more shallow energy levels. For example, gold (Au), a transition metal, creates a localized recombination center, and even a minute concentration (one part per billion) of it is capable of seriously intensifying the leakage current associated with the transistor. This aforesaid recombination of electrons and holes, governed by SRH statistics, has paramount impact on the effective lifetime of the semiconductor devices. The most substantial leakage currents emerge from trap levels near the middle level of the bandgap, that possess a deep potential well, while elements such as B, Al, Ga (column III) or P, As, Sb (column V) produce energy levels that are located near the band edge [21]. The very initial discussion pertaining to kinetics of this sort

recombination process took place in a work by Shockley and Read in their famous paper [22], and similar results were also argued by Hall [23].
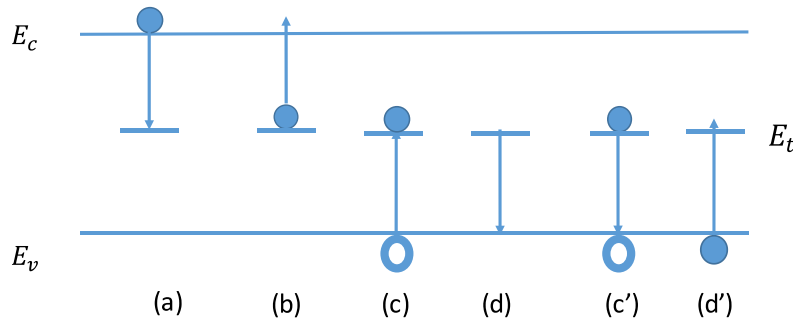
Figure above portrays four different possible ways that SRH recombination may take place, which are described in detail below.

(a) A capture transition wherein the empty trap center captures an electron from the conduction band.

(b) The inverse of (a) where the aforesaid trapped electron is released from the mid-level center.

(c) Hole recombining with a trapped electron that resides in a mid-level energy.

(d) The inverse process of what is depicted for (c).

(c') Electron transitioning into an unoccupied space by electron situated in the valence band.

(d') Promotion of an electron into mid-level trap state.

Since their work [22] is aimed to statistically define the working principles of such recombination events, the math associated with SRH merits a brief discussion. Equation below describes the recombination rate pertaining to an electron captured by a trap level.

$$U_{e-capture} = B_n n D_{it}(1 - f_t) \tag{8}$$

, where B_n, n, D_{it}, and $(1 - f_t)$ represents a quantum mechanical constant, related to this transition, electron concentration in the valence band, density of trap states, and the probability of a trap band not being occupied. And the electron emission, as shown by Figure 9 (b), is given as follows.

$$G_{e-emission} = B_n n_t D_{it} f_t$$

, with n_t representing the electron concentration in the trap state, and as expected the probability of these electron being occupied there, f_t, has to be also taken into account. In real life situations, the capture and emission rates related to electron and holes is expected to be different, which is dictated by the affinity of the trap for electron and holes. This being the case, however, the steady state conditions will prevail that the net rate of capture by traps for hole and electrons must be equal to each other so that there will be no build-up charges on the traps. This allows one to derive the following relationship by using the fact that $\tau_{n,SRH} = \frac{1}{v_n \cdot \sigma_n D_{it}}$, with v, σ being mean thermal velocity of an electron and the capture cross section respectively.

$$U_{SRH} = \frac{np - n_i^2}{\tau_{n,SRH}(p + p_t) + \tau_{p,SRH}(n + n_t)} \tag{9}$$

What is governed by the Shockley-Read-Hall statistical relationship above is the expression for electron and hole recombination via a single level trap site [24]. As can be observed,

22

one significant driving force for the SRH recombination is the deviation of carrier concentration from the thermal equilibrium value (n_i), which is denoted by the term ($np - n_i^2$), bringing the injection dependence of this recombination mechanism. Therefore, this injection dependence can be used to highlight special conditions different kinds of defects. For instance, for the case of deep-level traps, and under low-injection conditions, τ_{SRH} is equal to $\tau_{n,SRH}$ in an n-type material, $\tau_{p,SRH}$ in an p-type material, implying that there is direct relationship between the minority carrier lifetime ($\tau_{n,SRH}, \tau_{p,SRH}$), and the recombination rate [20]. On the intuitive side of things, for recombination events to take place, usually, both carriers have to be present locally, which suggests that the SRH recombination rate is the highest when $n \approx p$.

2.2.3.2 Surface Recombination

The surface of a semiconductor device and the interface between two neighboring crystal regions constitute the biggest disturbance of symmetry in a crystalline structure. This can appear due to a variety of reasons such as non-saturated "dangling" bonds, or impurities residing at the interface creating surface continuum states within the bandgap of the material. Due to the nature of surface recombination process, SRH theory governs this process as well for a single interface state. Aforementioned continuum of states requires the integration of equation (9) over energy so that contribution from all interface states within the bandgap is covered with the below equation.

$$\int_{E_V}^{E_c} D_{it} \frac{p_s n_s - n_i^2}{v_p \sigma_p (n_s + n_t) + v_n \sigma_n (p_s + p_t)} \qquad (10)$$

, where variables with s subscript represents the carrier distributions at surfaces. One other important metric to define is the "fundamental" speed at which these carriers are recombining at surfaces, that is governed by the following relationship.

$$S_{no} = \int_{EV}^{Ec} D_{it} \, v_n \sigma_n dE. \tag{11}$$

Note the importance of the term "fundamental" which is only concerned with chemical passivation at the interface, neglecting the impact of charge passivation. Since usually there is no direct access to surface carrier concentration, p_s, n_s, it is convenient to define an effective surface recombination velocity, S_{eff}, as a function of excess carrier concentration at the edge of the quasi-neutral region, Δ_{n_d} [25].

$$S_{eff} = \frac{U_s}{\Delta_{n_d}} \tag{12}$$

As a consequence of the relationships delineated by (11) and (12), there are two separate physical mechanisms to diminish the impact of surface recombination [20]. These solutions may come in many flavors, but in essence these deal with either saturating the dangling bonds at the interface or shielding the minority carrier from the interface so that only majority carrier is present locally. Though the subtleties of passivation properties will be covered in a separate section, it is important to highlight that the creation of "built-in" electric field can be provided by either (a) implementation of a doping profile right beneath the surface of semiconductor or (b) what is known as field effect passivation by means of charge presence at the interface after deposition of insulator

layers on a semiconductor. As will be emphasized in detail later, the deposition of silicon dioxide, unsaturated bonds are passivated with oxygen and hydrogen atoms.

2.2.4 Emitter Recombination

Though emitter recombination is not a separate physical phenomenon, it plays quite a crucial role in preparing symmetric test structures for the evaluation of different passivation layers. The modeling of this heavily doped layer is a fairly complicated task since it involves numerous physical events. For instance, non-uniform doping profiles, combined with the presence of a dead layer (following the diffusion), need to be taken into account which complicates the calculations. The treatment of highly doped surfaces possess a variety of different features that separate them from a lightly doped bulk material. These effect include degeneracy, free carrier absorption (usually kicks-in in longer wavelengths), and bandgap narrowing. To go about these aforementioned issues, a couple of assumptions is done. First, owing to the heavily doped nature of the surface, it is likely that Auger recombination will dominate, thus recombination lifetime in the emitter is assumed to be injection independent and can be expressed as follows.

$$J_{recombination} = J_{o-emitter} \frac{np}{n_i{}^2} \tag{13}$$

, $J_{o-emitter}$, n, p refer to emitter saturation current density (mA/cm^2), electron and hole concentrations at the base of space charge region. Therefore, this perception enables the analysis of the emitter region as a separate surface entity residing at the base of the space-charge region. By merging Eq. (12) and (13), one can write the following [26].

25

$$S_{effective} = J_{o-emitter} \frac{N_A + \Delta n}{q n_i{}^2} \qquad (14)$$

, N_A is the doping density.

The reasons that makes the analysis of this recombination current analysis really effective is that low injection conditions apply to these regions and material parameters do not vary as a function of injection level [27].

2.2.5 The Effective Lifetime

Solar cells are a prime example of the "leaky bucket" process, wherein the ultimate operation performance of the device is limited by the weakest link. Even this might be the case, in the general sense different recombination processes contribute independently to the effective lifetime, so that the following equation can be written.

$$\frac{1}{\tau_{eff}} = \frac{1}{\tau_{bulk}} + \frac{1}{\tau_{eff}} \qquad (14)$$

, which can be written as follows.

$$\frac{1}{\tau_{eff}} = \left(\frac{1}{\tau_{radiative}} + \frac{1}{\tau_{Auger}} + \frac{1}{\tau_{bulk,SRH}} \right) + \frac{1}{\tau_{Surface,SRH}} \qquad (15)$$

, as can be deducted, just like a parallel connected resistors, the process with the highest frequency, or lowest lifetime, will dominate the overall impact on the effective lifetime. On the practical side of things, certain recombination processes can be forced to be negligible so that the

26

one of interest can be distinguished. For example, high quality bulk materials, monocrystalline with high resistivity, are used to study the impact of surface recombination given that the bulk recombination is minimized.

CHAPTER 3 - APPLICATIONS OF METROLOGY

3.1 Biased-Photoluminescence

An alternative method to image essential variables like dark saturation current density, series resistance, and cell efficiency is introduced in this dissertation. This approach combines the terminally connected diode model with a modified technique for extracting the spatially resolved ideality factor of the cell under non-open-circuit conditions. Following a description of the steps governing the principles of this parameter imaging approach, we explore potential benefits of this technique and how it may improve upon existing methods [28].

3.1.1 Introduction

With the recent appeal to the combination of the electroluminescence (EL) and photoluminescence (PL) measurements, also known as biased-PL, due to its paramount speed capability, a number of research groups came up with different methods to assign physical relevance to each pixel in the recorded images [29-31]. Biased-PL is a much faster way of obtaining spatially resolved information about crystalline silicon (c-Si) photovoltaic (PV) cells than scanning, point-by-point measurements. The first attempt to image the series resistance of c-Si PV cells via PL imaging was made by Trupke *et al.* [29]. Two subsequent approaches to imaging R_S and other PV cell parameters merit a brief discussion.

The elegant theoretical background enabling the understanding of voltage and illumination contributions to the PL image was derived by Glatthaar *et al.* [30], which also removed the necessity for the secondary short-circuit image required in [29]. However, though different recombination features will appear in the current density image (J_{xy}), this method assumed that

each diode in the terminally connected model was behaving as an ideal one. Another approach is the integration of the effective ideality factor into the model. Shen *et al.* [31] circumvented this by starting with an arbitrary global ideality factor (*m*), varying it until the mean of the calculated current density map matches the globally measured current density at maximum power (J_{mp}). As an alternative to using an empirically determined global ideality factor, we propose the incorporation of a spatially resolved ideality factor, determined using PL images collected at different illumination levels [32] and with corresponding biases applied, in calculating local cell efficiency. As an additional exploration to [33], this paper provides more detailed comparison of the results obtained when using two previous methods, [30], [31] to our proposed approach utilizing the spatially resolved ideality factor for biased-PL analysis. The aim of this work is to introduce a new way of determining spatially resolved ideality factor at maximum power point and this variable is fed into the algorithm to yield an efficiency map. The advantage of this new approach will be discussed in experimental details section when we compare the different regions of the solar cell.

3.1.2 Theory

Since this study is aimed at attributing a physical quantity to a relative PL intensity image, it is meaningful to review the underlying principles of the equations exploited in the calculations. As mentioned by Trupke *et al.* [29], and shown mathematically by Glatthaar *et al.* [30], an image taken at open-circuit and low illumination conditions (i.e., 0.15 suns) is required, and the PL intensity can be expressed as follows.

$$\varphi(x,y)_{low-light} - B(x,y)I_{low-light} = C(x,y)\exp(\frac{V(x,y)}{V_T}) \qquad (16)$$

,where $\varphi_{(x,y)_{low-light}}$ is the PL image under low light conditions, $C_{(x,y)}$ is the calibration constant, $B_{(x,y)}$ is the second calibration constant taken at short-circuit and scales with the illumination intensity, $I_{low-light}$, in terms of number of suns, and V_T is thermal voltage.

Variable	Description
J_{mp}	Global current density at maximum power point.
m	Global ideality factor which does not have any spatial information. It is determined empirically.
$V(x, y)$	Spatially resolved local junction voltage.
$C(x, y)$	One of the two local calibration constants used to ascribe a physical relevance to an uncalibrated PL image. This is obtained at low illumination intensity and at open-circuit conditions where the voltage gradient due to resistance effects can be neglected.
$B(x, y)$	The second calibration constant. This one is obtained at 1 sun excitation and at short-circuit conditions to account for the so-called diffusion-limited carriers.
$\varphi(x,y)$	Uncalibrated photoluminescence image.
I	Illumination intensity used to represent the number of suns used during the excitation which is a scaling factor for the second calibration constant, $B(x, y)$.
$R_s(x, y)$	Spatially resolved series resistance map determined in accordance with the circuit model described.
$J_0(x, y)$	Dark saturation current density map determined in accordance with the circuit model described.
$V_{terminal}$	Global terminal voltage that is measured at the terminal of the solar cell during each measurement.
$m(x,y)$	Spatially resolved ideality factor image, which in this work is determined at open-circuit and maximum power point.
J_D	Global diode current.

R	Global recombination rate.
G	Global generation rate.
q	The electrical charge which has a value of -1.602×10^{-19} Coulombs.
$I^*(x,y)$	This term stands for the uncalibrated PL image corrected by the effect of the diffusion-limited carries.
J_p	Photo current density as denoted in the one-diode equation.
m_{rec}	Global ideality factor that is used to fit the I-V curve for the whole range of voltage points instead of the local slope.
m_{emp}	Empirically determined ideality factor. This was determined by iteratively maintaining the calculations while making sure the average value of the current density map matches the global current density value.

These two constants are determined exactly in the same way as in [30]. Under these conditions, one can assume little spatial variation in the voltage over the entire the wafer enabling the calculation of a calibration constant (C) that is independent of bias and illumination. Of course, there will be a trade-off between the required acquisition times, which is an issue for low injection levels, and how accurate the assumption of no lateral voltage gradient is. It was illustrated by Höffler *et al.* [34] that even 0.19 suns could yield significant errors (≈ 5 mV) in the calibration procedure, which was shown to be a low enough illumination. To reconcile with this trade-off argument between the exposure time and the accuracy in voltage calibration, we acquired the low-illumination image at 0.15 suns since exposure time was not a major concern for this work.

Therefore, the calibration constant can be given by the following equation,

$$C(x,y) = \left(\varphi(x,y)_{low-light} - B(x,y)I_{low-light}\right)\exp(\frac{-V_{low-light}}{V_T}) \qquad (17)$$

where $B_{(x,y)}I_{low-light}$ accounts for the so-called diffusion limited carriers, and $I_{low-light}$ stands for the number of suns used in the excitation [29]. To elucidate the meaning of this correction, consider a cell operating at short-circuit and under illumination. Excess electrons are able to leave the circuitry from the *n*-type region and meet a hole somewhere in the material to recombine radiatively. Even though the quasi-fermi levels do not split at the *p-n* junction, which constitute the implied voltage coming from the modeled diode, the photon emitted as a result of this radiative recombination process is still detected by the PL system. This is why this contribution, scaling with illumination level, should be subtracted from the original PL image taken at an arbitrary condition. Equipped with two of the calibration constants required for the biased-PL experiments, one could proceed to the circuit model, in which the solar cell is divided into separately operating diodes, each of which is connected to the terminal with its own series resistance.

$$V_{terminal} - V(x,y) = R_s(x,y)\left\{J_0(x,y)\,exp\left(\frac{V(x,y)}{mV_T}\right) - J_G\right\} \qquad (18)$$

, where J_G is the photogenerated current and m stands for the ideality factor. An interesting thing to note here is the fact that with EL measurements, since the J_G term does not exist, there needs to be further assumptions to decouple the series resistance $R_{s(x,y)}$ and dark saturation current density $J_{0(x,y)}$ [30]. This J_G term, just like in [30], is assumed to be equal to short-circuit current density of the solar cell. Future plans associated with this assumption are mentioned in the conclusion part of this study. Though it is not considered here, another interesting point could be

the variation in ideality factor, m, as a function of applied voltage, which is varied to solve for $R_{S(x,y)}$, and $J_{0(x,y)}$.

The first demonstration of ideality factor imaging was by Hameiri *et al.* [32], wherein open-circuit PL images collected at different illumination levels were used to calculate $m_{(x,y)}$ and can be used to solve for each pixel individually instead of using an empirically determined global ideality factor. In this work, $m_{(x,y)}$ is determined at V_{mp} rather than V_{oc}. The diode equation under illumination and applied voltage reads:

$$J_D = q(R - G) \tag{19}$$

where J_D, R, G, q stand for diode current (A·cm^{-2}), recombination rate (cm^{-2}·s^{-1}), generation rate ($cm^{-2}s^{-1}$), the electrical charge (-1.602×10^{-19} Coulombs) . Just like the elaborate model used in [35] to calculate the generation current, and under the assumption of uniform illumination on the cell plane, one can determine each rate contribution in Eq. (19). Furthermore, with the correct generation rate, and knowing the current density at maximum power point for each illumination level, one can write the following,

$$m(x,y) = \frac{J_G - J_{mp}}{\varphi_{(x,y)}} \left(\frac{d\varphi_{(x,y)}}{d(J_G - J_{mp})} \right) \tag{20}$$

where $m_{(x,y)}$ and J_{mp} represent the spatially resolved ideality factor at maximum power point and current density of the cell at maximum power point, respectively. Within the scope of this work, we assumed the generation current and diode current to be spatially uniform, even

though recombination features that have spatial relevance will be reflected in the PL intensity. The assumption with the latter is supported by the monochromatic spatially uniform laser illumination. The second assumption of uniform current is discussed in the experimental details part of this work. Here, we utilized the software that is freely available online called OPAL 2 to calculate the generation current under monochromatic illumination with wavelength of 808nm for cells with iso-textured surface, since we used multicrystalline cells in this case. To obtain this current we input the flux associated with the excitation, $2.82 \cdot 10^{17} \text{cm}^{-2} \cdot \text{s}^{-1}$, and the software outputs the generation current.

This modification is appealing since it accounts for a situation where current extraction occurs, and ideality factor is shown to fluctuate for different bias conditions [32].

To maintain the above procedure, one can vary the illumination level and keep track of the change in maximum power point voltage values associated with each illumination level.

3.1.3 Experimental Details

In this work, illuminated *I-V* measurements and PL images were acquired on a 243 cm^2 multicrystalline Si 200 μm thick 1 $\Omega . cm$ Al-BSF cell. Illuminated *I-V* measurements were performed at 1 sun using two different systems: (1) a PV Measurements systems featuring a class AAA solar simulator matched to an AM1.5G spectrum; and (2) a commercial BT Imaging LIS-R1 featuring a monochromatic laser light source with a wavelength (λ) of 808 nm. This laser imaging system also includes a 1-megapixel silicon CCD camera that is aimed to capture the luminescence coming out of the solar cell. To distinguish the reflected signal due the laser excitation, 920nm high-pass filter is used. In this work, 1 sun irradiance with the laser source is

defined as the intensity at which the measured short-circuit current (I_{sc}) is approximately equal to that measured with the solar simulator at AM1.5G. For the cell measured here, a photon flux of $2.82 \cdot 10^{17} \, cm^2 \cdot s^{-1}$ for the laser source was used. Table 3 below provides cell parameters extracted from these *I-V* measurements with the two systems featuring different incident spectra. All the PL imaging in this work is done with LIS-R1 system.

Table 3. Cell parameters extracted from *I-V* measurements under two spectra.

Incident Spectra	J_{mp}(mA·cm^2)	V_{mp}(V)	I_{sc}(A)	V_{oc}(V)	Efficiency
AM1.5G	31.9	0.515	8.32	0.614	16.42%
λ = 808 nm	31.9	0.521	8.31	0.621	16.62

Due to the pixelated nature of the problem, adding another piece of spatial information should increase the fidelity pertaining to highlighting the contrast among different points on the cell. Since efficiency is reported at the maximum power point, the idea brought into attention by Eq. (20) should complement this addition of information to the problem. To implement this solution into the biased-PL scheme, multiple images at different illumination levels with their corresponding maximum power point voltage values are taken. These constitute the slope term highlighted in Eq. (20). Incorporating the generation rate at 1 sun and the current density at maximum power point into the analyses yields the spatially resolved *m* at the desired operating point, which is 1 sun and $V_{terminal} = V_{mp}$

As pointed out in Fig.10, the linear relationship, with an R^2 value of 0.998, between the PL intensity and ($J_G - J_{mp}$) supports the idea proposed in Eq. (20). Though it will not be considered here, fluctuation in the ideality for two different bias conditions might be incorporated into the two

equations that will be used to solve for $R_{s(x,y)}$, and $J_{0(x,y)}$. To create variation in the current

extraction values, we used the voltages corresponding to 25% of the I_{sc} value and one at V_{mp}.
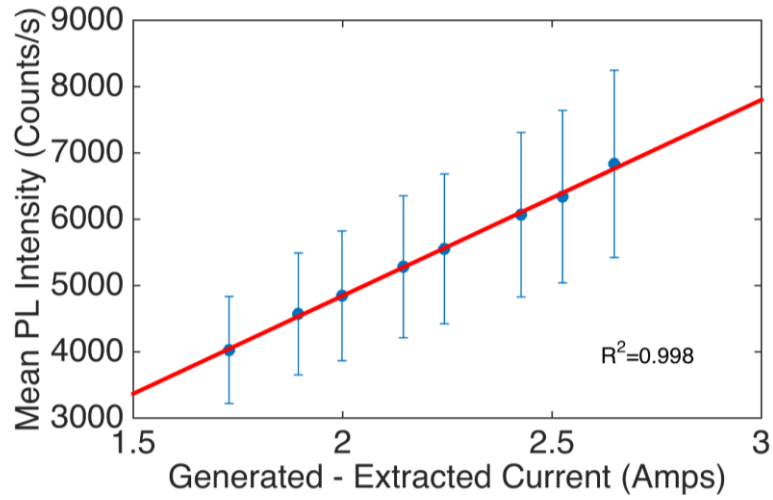
Figure 10 Mean PL intensity vs. difference in generated and extracted current. $(J_G\text{-}J_{mp})$ term is multiplied by the area of the cell, which is shown in the x-axis. The error bars extend one standard deviation away from each data point.
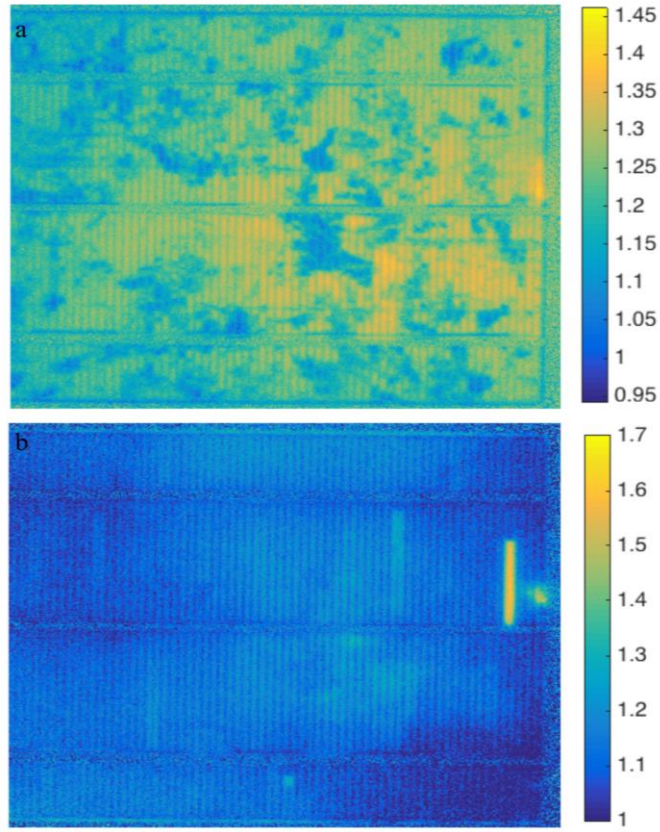
Figure 11 Ideality factor images acquired at different electrical bias conditions, including: (a) at open-circuit (i.e., no electrical bias); and (b) the maximum power point ($V_{terminal}$ = 0.521 V).

To get the ideality factor $m_{(x,y)}$ at $V_{terminal} = V_{oc}$, the same procedure in [32] is followed. This is achieved by changing the photon flux coming out of the laser source, and recording the PL images while the terminal is at open-circuit conditions. The ideality factor maps associated with the $V_{terminal} = V_{mp}$ and $V_{terminal} = V_{oc}$ conditions are in Fig.11.

There are some subtleties with the resistance effects observed in Fig.11 (b). The general description of the ideality factor relates to the exponential relationship between the recombination current and the voltage across the *p-n* junction. For example, when Shockley-Read-Hall is the dominant type of recombination in depletion region or at high injection when both carrier types

38

present at comparable concentrations, this term will be equal to 2. And low-injection m_{rec} could be equal to 1, when one carrier type dominates the recombination [36].

$$J \approx \exp\left(\frac{V}{m_{rec}V_T}\right) \qquad (21)$$

where m_{rec} could be used to fit I-V curve. Local ideality factor, on the other hand, pertains to the local slope of the $\ln(I)$-V curve. Moreover, this slope term may not relate to the exponential relationship described in Eq. (21) due to lateral transport effects created by series resistance [36]. The fact that we observe resistance effects in Figure 11 could be related to this lateral transport effect or the spatially uniform current density assumption made in (19).

3.1.4 Comparison of different methods and experimental results

Due to their spatial variation, many studies on extracted cell parameters from PL images have focused on multicrystalline Si PV cells. These spatial inhomogeneities may reflect different loss processes occurring within the cell and are mathematically governed by Eq. (18), which incorporates ideality factor. To highlight the importance of the different loss mechanisms, two existing efficiency imaging methods will be considered and compared against the technique we propose. Fig.13. features images of efficiency, dark saturation current density, and series resistance using all three techniques.

Before we introduce the results acquired from the technique using a spatially-resolved ideality factor, we would like to address the contrast in the two existing models that incorporate a single, spatially uniform m over the entire cell (left and middle columns of Figure 13). The method

assuming a unity ideality factor ($m = 1$) from Glaathar *et al.* [30] and the method using an empirically determined ideality factor (m_{emp}) by Shen *et al.* [31] reveal significantly different results, with a difference in absolute efficiency of almost 2% among certain pixels. This region is highlighted by the purple box in Figure 13. This gap between the two methods grows as the m_{emp} used to match the global J_{mp} value deviates further from its ideal value of one. This particular cell has a high m_{emp} of 1.63. The mean values of the efficiency images are 17.5% and 16.6% for the ideal diode and m_{emp} techniques, respectively. Of course the mean value of 16.6%, obtained using the m_{emp} technique [31], exactly matches the cell's efficiency measured from an *I-V* curve at 1 sun, since the technique relies on empirically matching J_{mp}. Flow chart below is aimed to portray the differences between the three methods.
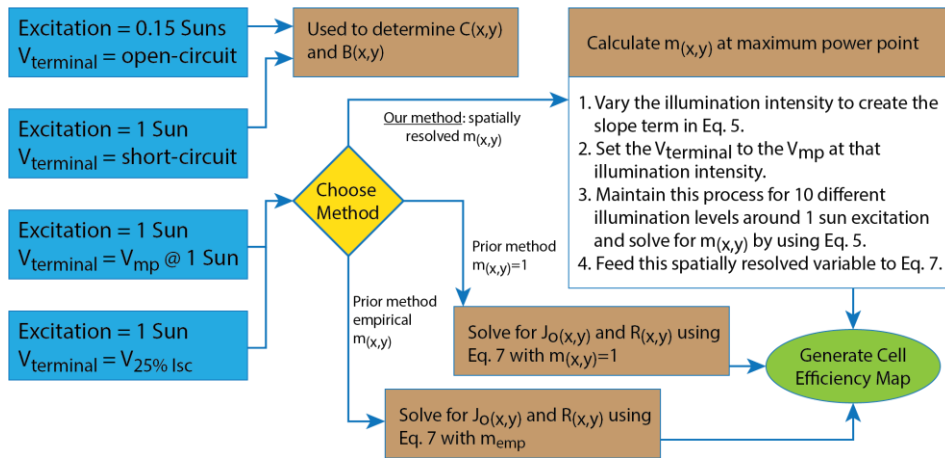
Figure 12 Methodology of different algorithms used in this work.
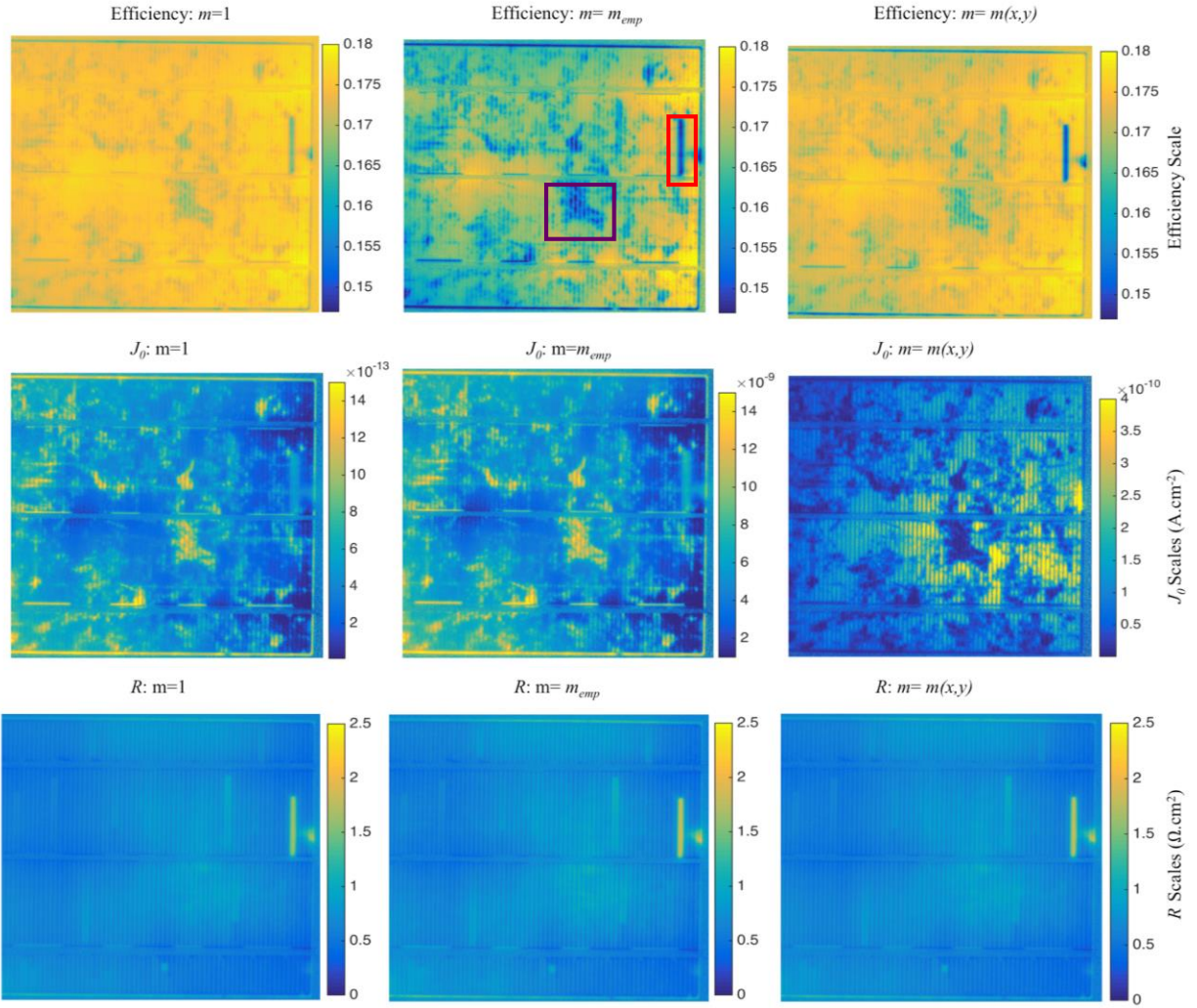
Figure 13 Efficiency (top row), dark saturation current density (middle row), and series resistance (bottom row) images obtained on the same 243 cm^2 multi-crystalline Si Al-BSF cell. Three different methods of incorporating ideality factor were used in the solution of these parameters, including: (1) the assumption of an ideal diode ($m = 1$) (left column) [30]; (2) an empirically determined ideality factor (m_{emp}) (middle column) [31]; and (3) a spatially resolved ideality factor model $m_{(x,y)}$. For the efficiency images, a rectangular region with high series resistance is highlighted with a red box and a crystal grain with high recombination is highlighted with a purple box for statistical analysis.
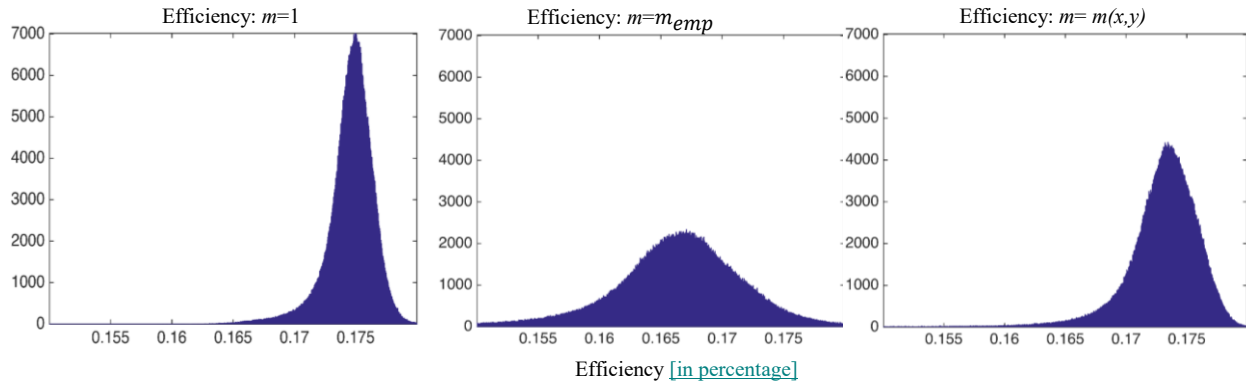
Figure 14 Histogram of the efficiency images for the three techniques used in this work. X-axis represents the efficiency in percentage while the y-axis stands for the number of points in the image that has the corresponding efficiency value.

The technique of using a spatially-resolved $m_{(x,y)}$ proposed here (right column of Figure 13) results in a mean efficiency of 17.3%, a value in between the other two techniques.

Furthermore, since Shen *et al.* match their mean value of the current density map to the global J_{mp} value, measured by other means such as an *I-V* test, the mean value of the efficiency map will always match the global efficiency value. This way of mapping these physical variables may mix the behavior of two concurring loss mechanisms, namely the recombination and series resistance. This was actually the key promise of Glaathar *et al.*, since that paper wanted to improve upon EL-based treatments by the introduction of the clear separation of dark saturation current and series resistance effects.

Figure 14 illustrates the histograms for the efficiency maps for the three different methods, considering the region only where the cell exists. Quite interestingly, the iterative nature of the calculations in [31], which is based upon spatial averaging, makes the distribution follow a Normal distribution-like shape. This was not the case for the newly introduced method here, which basically followed a very similar trend as in the ideal-diode model, which seem to not modify the

42

efficiency distribution. To gain a better understanding of the contrast that can be gained from the adoption of this $m_{(x,y)}$ term, mean values of the regions with significant recombination and resistance losses were analyzed.

Table 4. Mean values of series resistance and efficiency for the regions highlighted in Figure 4 with large series resistance losses (red box) and recombination losses (purple box).

	$m = 1$		m_{emp}		$m\,(x,y)$	
	Mean R ($\Omega \cdot cm^2$)	Mean Eff.	Mean R ($\Omega \cdot cm^2$)	Mean Eff.	Mean R ($\Omega \cdot cm^2$)	Mean Eff.
High resistance (red box)	1.41	10.1%	1.56	9.1%	1.52	9.3%
High recomb. (purple box)	0.83	17.0%	0.92	15.5%	0.85	16.6%

As can be seen from the above table, the method using m_{emp} [31] and the one using $m_{(x,y)}$ yield similar R values for the high resistance rectangular region highlighted in red in Fig. 3., 1.56 vs. 1.52 $\Omega \cdot cm^2$. However, when it comes to the analysis of the region with a high recombination crystal grain, a discrepancy between these two methods arises. The m_{emp} method gives an increased series resistance in these regions when compared to the other two methods. The $m_{(x,y)}$ method was able to create a similar resistance value for the stripe-like region without increasing the resistance value of the grain boundaries. This difference between the m_{emp} and the $m_{(x,y)}$ methods occurs due to the averaging nature of the earlier approach. Equations used to determine the efficiency, series resistance, and reverse saturation current density are as follows:

$$\overbrace{V_{terminal} - V_T.\ln\left(I^*_{(x,y)}\right) + V_T.\ln\left(C_{(x,y)}\right)}^{K_i} = \overbrace{-\widehat{J_p}}^{A_{i,1}}.\overbrace{\widehat{R_{(x,y)}}}^{S_1} + \underbrace{R_{(x,y)}.J_{o(x,y)}}_{S_2} . \underbrace{\left\{\frac{I^*_{(x,y)}}{C_{(x,y)}}\right\}^{\frac{1}{m_{(x,y)}}}}_{A_{i,2}} \tag{22}$$

,where $I^*_{(x,y)} = \varphi(x,y)_{low-light} - B(x,y)I_{low-light}$ and J_p stands for photo current density. Just like in [30], Eq. (21) yields a system of linear equations, and with two images, it can be used to solve for $R_{s(x,y)}$ and $J_{o(x,y)}$. This system of linear equations come in the form of $K_i = \sum A_{i,j}.s_j$. We followed a very similar formulation in [30], though we solve for $C_{(x,y)}$ using Eq. (16) and of course $m_{(x,y)}$ at maximum power point from Eq. (19) is included. And finally the efficiency is described as follows:

$$\eta_{(x,y)} = \frac{V_{mp}.J_{mp}_{(x,y)}}{0.1\ W.cm^{-2}} \tag{23}$$

, where $J_{mp}_{(x,y)} = \frac{V_{term} - V_{(x,y)}}{R_{s(x,y)}}$, $0.1\ W.cm^{-2}$ stands for the 1 sun illumination power density, and V_{mp} is the maximum power point voltage at 1 sun. This is similar to the relations described in [31]. Before the concluding remarks, it is worth mentioning the possible effects of horizontal balancing currents that especially dominate at open-circuit voltage. The $J_0(x,y)$ at the center right of Fig. 13. is obtained by combining the open-circuit voltage map with the ideality factor map at open-circuit condition with the following relationship:

$$J_{o(x,y)} = J_{sc} \cdot \left[\exp\left(\frac{V_{oc(x,y)}}{m_{(x,y)}.V_T}\right) - 1\right]^{-1} \tag{24}$$

44

One possible reason to why one observes lower ideality factor values for the grain boundaries could very well be attributed to the existence of horizontal balancing currents [37]. Since the "turn-on" voltage for the diode that corresponds to a grain boundary region will be lower than the surrounding pixels, there will be balancing currents flowing from the diodes with higher turn-on voltage to the lower ones. This direction of current will assign a higher ideality factor value to the diodes with higher turn-on voltage, solely due to horizontal balancing currents.

3.1.5 Conclusion

As it is highlighted within the flow of this work, integrating the spatially resolved ideality factor into the model given by Eq. (19) yields drastically different values for the device parameters. The method introduced here seems to distinguish different loss mechanism occurring within the cell. Rather than assuming a fixed ideality factor value for the whole cell, this method provides direct pixelated calculation of $m_{(x,y)}$. As highlighted in section IV, this makes it possible, to distinguish resistance and recombination loss mechanisms by assigning ideality factor values to each point on the cell, instead of providing higher resistance values for recombination active regions, which would be the case for spatially fixed m.

One issue that could appear with this analysis is the assumption of spatially uniform terminal current which, combined with spatially uniform generation rate, may mean a spatially uniform recombination rate, even though associated features will be captured in the PL image, both of which appear in Eq. (19). Circuit simulations will be done to find the root cause of resistance effects observed in Fig. 11(b).

Another key assumption made in most of the mapping methods is the spatially uniform light generated current, shown to be inaccurate by Höffler *et al.* [38]. In order to analyze what difference this factor will make in the extraction of physical parameters, we plan to incorporate spatial mapping of the J_{SC} term into our analyses using a novel, ultrafast quantum efficiency system. Finally, the validation of this method is planned through a correlation study using a DLIT-based technique.

3.2 Void Detection in PERC Cells with Photoluminescence Imaging

An image-processing method combined with Fourier analysis is introduced in this work as a rapid and highly-automated method of detecting rear contact voids in passivated emitter and rear contact cells (PERC). This approach utilizes photoluminescence (PL) imaging to locate the central point of the most detrimental type of voids and associate a void fraction to each cell in a manner of seconds. Acoustic microscopy and scanning electron microscopy are also used as complementary tools to confirm the presence of voids detection using PL imaging and provide more insight into the actual physical mechanism of what is observed in PL measurements [39].

3.2.1 Introduction

As the transition from standard full area aluminum back surface field (Al-BSF) cells to PERC becomes more pronounced, the need for industrially applicable and possibly in-line characterization of PERC cells turns out to be a relevant task. PERC cells lead to higher conversion efficiencies due to lower surface recombination and better light trapping. These are achieved by incorporating a passivating dielectric stack at the rear surface and locally opened rear contacts,

instead of a full-area BSF and Al back contact. The insertion of the dielectric layers provides a higher open-circuit voltage and improves the long-wavelength response of the cell by increasing the back-reflectance [40]. This structure is expected to gain major market share and practical roadmaps show the possibility of reaching efficiency values of 22% in high-volume manufacturing [41].

One possible challenge, as the carrier transport becomes two or three-dimensional for line and dot contacts, respectively, is the decrease in fill factor due to higher series resistance [42]. Another problem that has widely occurred during the production of these cells is the formation of voids around the local contacts [40, 43, 44]. This can be attributed to the Kirkendall effect, which governs the diffusion of atoms through vacancies. The formation of voids can be explained by several factors. As it was shown by the earlier work, as the contact spacing increases, the diffusion of the silicon atoms from the bulk to the aluminum matrix will become more likely [5]. This will also lead to a decrease in the thickness of the local back-surface field. Analysis from the same work also showed that, when there is a eutectic layer formed, silicon content in the Al-matrix diminishes, and instead the silicon from the Al-Si melt recrystallizes to form the BSF. This may lead to a void with BSF. Therefore, if the contact spacing is too large, there may not be enough silicon in aluminum to form the eutectic layer, which then could lead to a void without BSF. High diffusive behavior of silicon is alleviated by introducing Si into the paste prior to alloying, which will lead to higher silicon content in the Al-Si melt for better eutectic formation [44]. Furthermore, recent studies also suggested that the Kirkenall effect may not be the ultimate cause of void formation after all. Dressler *et al.* illustrated that, by tweaking the time intervals for both cooling and heating, the trend for void formation stay the same, which refutes the existence of Kirkendall effect [45]. Kranz *et al.* concluded, by measuring the thickness of BSF, that void formation takes

places during the re-crystallization while Al is still in the liquid phase. From there, it was observed that contact height influences the interaction between the Al-Si melt and silicon surface itself, the larger the contact height the smaller wetting of the silicon surface by the Al-Si melt [46]. Voids without the BSF will turn out to be the most detrimental ones in terms of effecting solar cells' conversion efficiency [43]. This is due to minority carriers not being shielded by the back-surface field and causing increased recombination at the rear side of the cell. This type of void will also cause increased series resistance since majority carriers need longer distances to reach a healthy contact to be extracted out of the solar cell.

A number of research groups came up with different detection mechanisms to detect voids. Urrejola *et al*. [47] provided the very initial study concerned with why the voids might be formed in PERC cells with the aid of energy dispersive x-ray spectroscopy EDS/EDX analysis. Dressler *et al.* used acoustic microscopy (AM) to illustrate the existence of voids combined with electroluminescence (EL) measurements [48]. As shown in [44], AM and EL analysis demonstrated that not all voids impact the cell performance in a significant way. Recently, Großer *et al.* utilized light-beam induced current (LBIC) quantify the electrical losses associated with void-related features, along with assigning an area fraction due to electrically active voids [49]. Given these previously published methods, a fast and reliable way of distinguishing recombination-active voids proves to be a relevant task. In this work, we present an automated way of detecting the most detrimental type of voids in a manner of seconds using open-circuit PL imaging in combination with our image-processing technique. In addition to this, we explore the nature of the using a combination of PL, AM and SEM imaging techniques conducted on the same sample.

PL intensity is a sensitive way of detecting local voltage values along the cell, which scales with intrinsic carrier concentration and the related constants, as shown below [50].

$$I_{PL} = \exp(\frac{V_{oc} \cdot q}{k \cdot T}) \cdot A_i \cdot B \cdot n_i{}^2 \qquad (25)$$

where q is the elementary charge, k is the Boltzmann constant, T is temperature, A_i is a scaling factor, and B is the radiative recombination coefficient for silicon. Due to the relationship between the local voltage and the recombination current [51], and given the high-resolution PL imaging systems currently available, PL imaging is particularly well-suited for detecting the recombination-active voids in PERC cells [52]. An example of an open-circuit PL image for a PERC cell with voids is shown in Fig. 15.
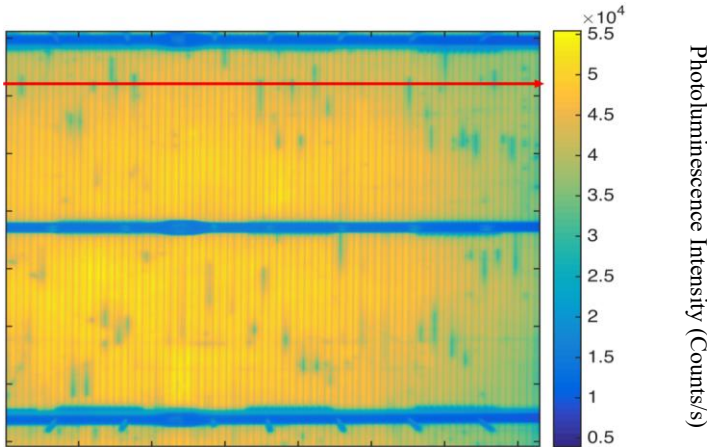
Figure 15 Open-circuit PL image of a PERC cell that has numerous voids.

Within the framework of this paper, we develop an image-processing technique that automatically detects these highly detrimental voids, which lack both a BSF and eutectic layer. To do so, we start by analyzing a line-scan taken perpendicular to the linear local back contacts of the

PERC cells used in this study, as highlighted by the red line in Fig. 15. The inverse of PL intensity is then calculated, where peaks in the line scan correspond to regions with a low PL intensity, as shown in Fig. 16(a). Here, it is difficult to distinguish the intensity reduction due to the front contact fingers, which are parallel to the linear local back contacts. To address this, we take advantage of the fixed spatial frequency ($\approx$1 mm or $\approx$10 pixel counts) of these front contact fingers. A Fourier transform is then performed on the inverse PL intensity to isolate the aforementioned frequency component and a cut-off filter is applied to remove these features. Following this step, a MATLAB-based image processing algorithm is used for the detection of the voids present in the PL image along with characteristics of the voids like their width and prominence, as shown in Fig. 16(b).
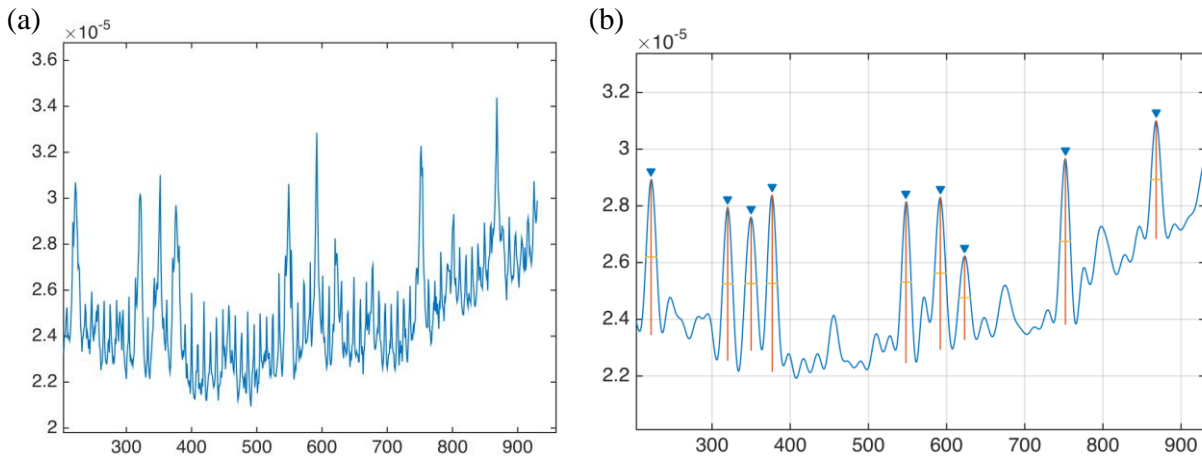
Figure 16 (a) Example of an inverse PL line scan taken perpendicular to the linear local back contacts for the PERC cell shown in Fig. 1. (b) The same line scan following a high-pass filtering process and feature detection step. The features with blue arrows above them indicate voids.

Quite significantly, the presence of front contact fingers can be eliminated from the analysis and void features can be isolated as a result of this procedure, as shown by the blue arrows in Fig. 16(b). To transform this detection procedure to the whole cell, one can repeat this analysis

for each row of pixels in the PL image. By doing this, and image of the voids can be created for the cell. Since the actual size of the linear local back contacts is known by the manufacturer ($\approx 60\mu m$, in this case), the localization of the central point of void can be used to calculate a void fraction for the cell of interest as well.

3.2.3 Experimental Details

In this work, we use industrial scale PERC cells, made from 156 mm x 156 mm p-type Cz wafers with a thickness of ≈180 μm. The cells were made using standard processes and feature linear local back contacts with a width of ≈60 μm and pitch of ≈1 mm. A BT Imaging LIS-R1 system with an 808 nm laser excitation source was used to collect one sun open-circuit PL images. One sun was established by adjusting the laser intensity until the short-circuit current density measured with the laser source matched the current measured with a calibrated class AAA solar simulator.

AM was performed on the PERC cell shown in Fig. 15 with a Sonoscan C-SAM® tool. The C-SAM technology used an ultrasound-pulsing 100MHz transducer that scans across the surface of the cell. A column of DI water from a jet attached to the transducer keeps the transducer coupled to the sample surface at all times, and makes it unnecessary to immerse the cell in water. Several thousand times a second the scanning transducer launches ultrasound into the surface and collects the echoes from within the sample. Only material interfaces such as silicon to aluminum reflect the ultrasound; homogeneous regions produce no echoes. When a pulse of ultrasound encounters a silicon-aluminum interface, very little of the ultrasound - about 0.4% - is reflected as an echo. The other 99.6% travels deeper into the sample. But if the ultrasound is traveling through

silicon and strikes a silicon-air interface (a void) the results are very different. The material properties (acoustic velocity and density) of silicon and air are so different from each other that very nearly 100% of the ultrasound is reflected. No other interfaces produce reflections as those from any solid-gas interface. The return echo signals have such high amplitude that the pixels in the acoustic image are typically bright white in monochrome acoustic images. Material interfaces from which less of the ultrasound is reflected appear in the acoustic image in varying shades of gray. In the analysis presented here, C-SAM technology from Sonoscan was used to detect and image voids. This technique is sensitive to both types of voids, those with a BSF and those without.

Cross-sectional SEM imaging was performed on the region highlighted by the red line in Fig. 15. The region of interest was laser scribed and cleaved, and cross-sectional SEM imaging was then performed using a Zeiss Ultra-55 FEG SEM equipped with a Schottky field emission source. The operating voltage was kept at 10 KV. Prior to that, double-sided conducting carbon tapes were used to make conducting contacts. All the images were obtained in secondary electron (SE) imaging mode wherein secondary electrons (SE) form the image of the surface providing useful information about its morphology and topography. Since the exact spacing between the contacts is known (1 mm), it was possible to identify each contact and compare it with both AM and PL measurements.

3.2.4 Results and discussion

Fig. 17(b) and (b) show the open-circuit PL image and a binary image of the void locations resulting from the analysis described in the Methodology section. The detected binary features, highlighted by the yellow points, correspond quite well to the what appear to be recombination-active voids at the local back contacts (i.e., voids without a BSF). This correspondence is verified

by acoustic microscopy and scanning electron microscopy images in Fig.18. Another PERC cell featuring few voids was also included in the experiments and analysis. This is clearly evident in both the open-circuit PL image and the resulting binary void image shown in Fig. 17(c) and (d), respectively. Using the known width of the linear local back contacts ($w_{contact}$=60 µm), and given their separation distance (1mm), the total the area covered by the back contacts can be calculated easily. Moreover, to associate an area fraction that exhibit the most detrimental type of void feature in a given cell, binary features highlighted in Fig.17. are used. To approximately translate the number of pixels that are detected to an actual length value, we determined how many pixels correspond to the actual size of the cell ($cell_{length/width}$=156mm) in the field of view of the camera, which in this case was around 960 pixels. This ratio (156mm/960pixels) was used to convert the binary features highlighted in Fig.17. to an actual length value. And the number of contact points, as shown in Eq. (26) is 156 since each contact is separated by 1mm. Finally, the area fraction that suffers from the voided regions is described as follows,

$$
Void\ Fraction \quad = \quad \frac{w_{contact} \cdot (\#\ of\ detected\ pixels) \cdot \left(\frac{\text{cell}_{length/width}}{\#of\ pixels\ corresponding\ to\ \text{cell}_{length/width}} \right)}{w_{contact} \cdot \text{cell}_{length/width} \cdot \#\ of\ contact\ points} \tag{26}
$$

By utilizing the methodology described in (26), the voided area fraction for the cell with dominant void features (Fig.17 (a)) turned out to be 2%, and 0.5% for the cell with few void features (Fig.17 (d)). What this means is that 2 percent of the local contact area of the highly voided cell exhibits the contacts that lack both the back-surface field and the eutectic layer. Based on scanning electron microscopy images of more than 30 contacts, we found that when the back-surface field is missing, the eutectic layer is also missing These results are further validated by

analyzing AM and SEM images in Fig.18. As can be seen in Fig.18III(c), in the absence of the

BSF, no eutectic layer is observed. As one might then expect, this cell also had a poor open-circuit

voltage value, 656mV (Fig.17 (a)), as compared to other cells, 660mV (Fig.17 (c)), studied in this

experiment with lower void fraction. The group of cells studied here, which are distinguished by

void impacts, had open-circuit voltage values ranging from 655mV to 660mV.

(a) Cell with many voids-PL image

(b) Cell with many voids-void image

(c) Cell with few voids –PL image

(d) Cell with few voids-void image
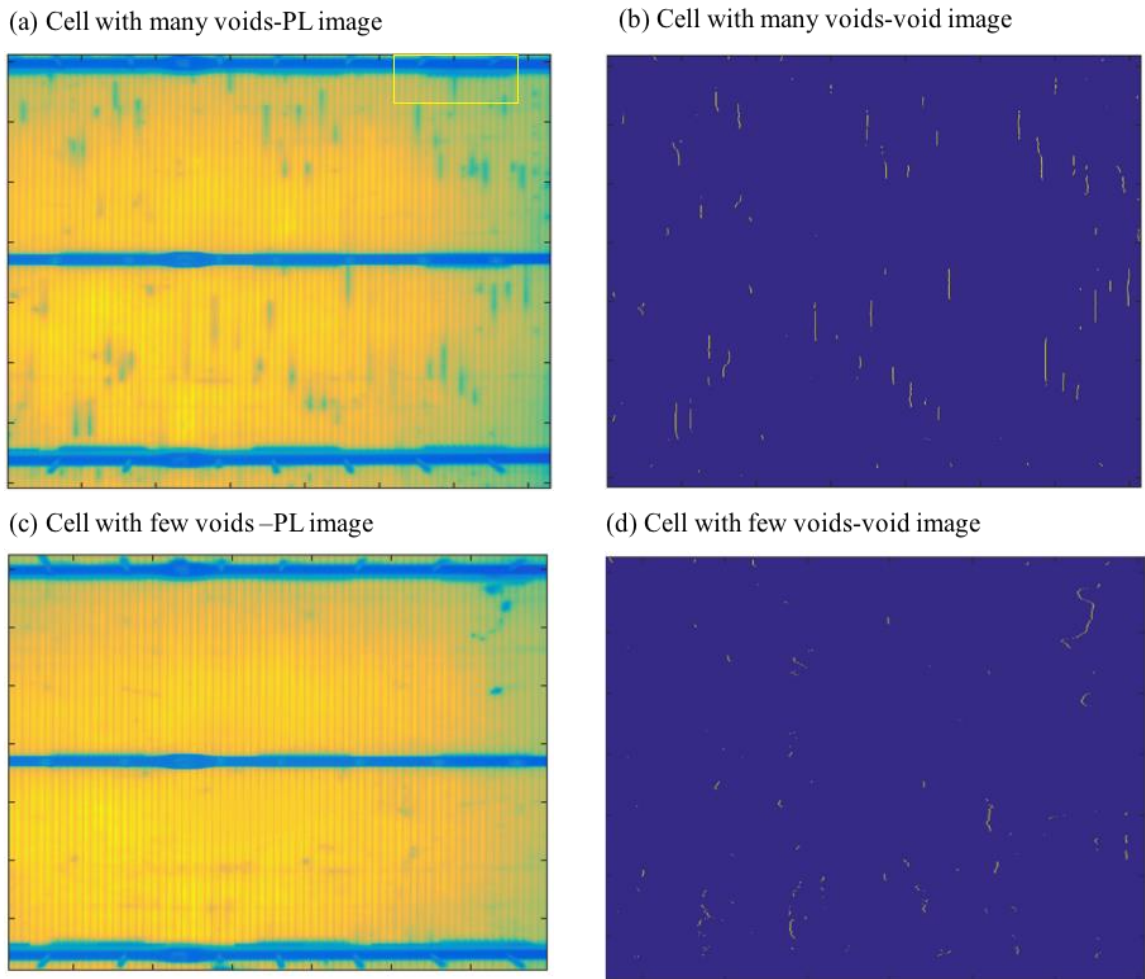
Figure 17 (a) One sun open-circuit PL image and (b) binary void image of the PERC cell with numerous voids. (c) One sun open-circuit PL image and (d) binary void image of the PERC cell with few voids.

To identify the type of voids present, an AM image was also obtained for the PERC cell

with numerous voids. A zoomed-in open-circuit PL image and corresponding AM image for the

same region of interest, highlighted by a yellow box in Fig. 17(a), are shown in Fig. 18(a) and (b). As pointed out previously, the open-circuit PL images are sensitive to the voids without a BSF (most detrimental - resistive and recombination losses), while the AM image is sensitive to both void types (with and without a BSF). In both images, three locations are highlighted. Location I features a void with a BSF (less detrimental – resistive loss only), so it doesn't appear in the PL image but it is captured in the AM image. Location II is a good contact, so it doesn't get detected by either technique. Finally, location III is the high recombination void without a BSF, so it shows up in both the PL and AM images. The cross-sectional SEM images shown in Fig. 18(c) clearly backup these results. Voids are clearly present at locations I and III, and while you can clearly see the BSF in locations I and II, there is no BSF in location III.
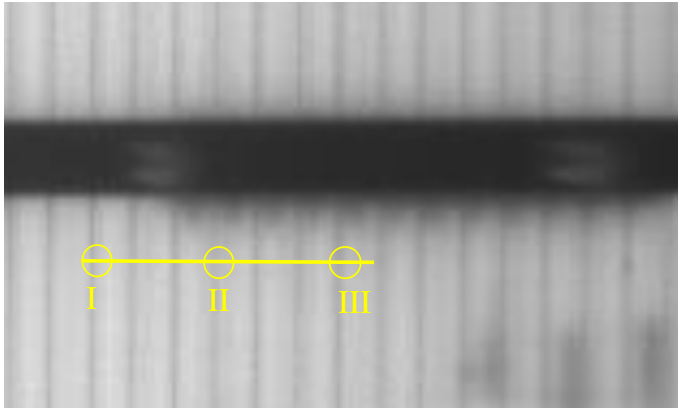
(a) Open-circuit PL image
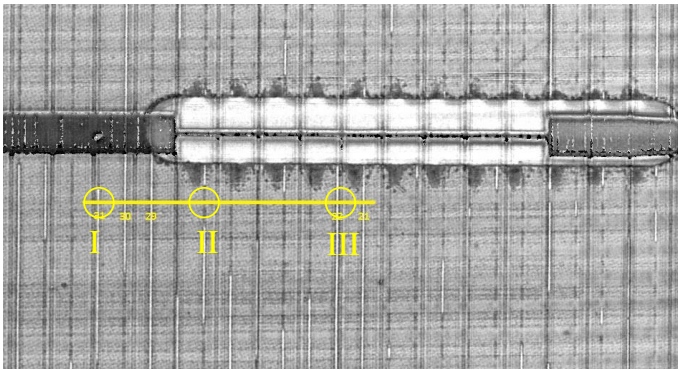
(c) SEM images

I. Void with BSF
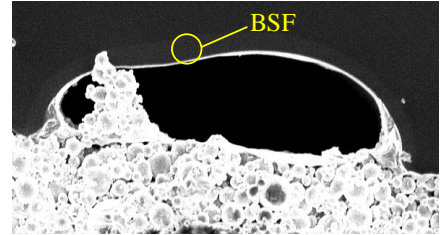
II. No void – good contact
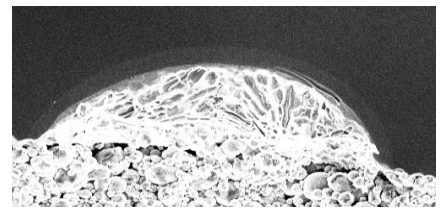
III. Void without BSF
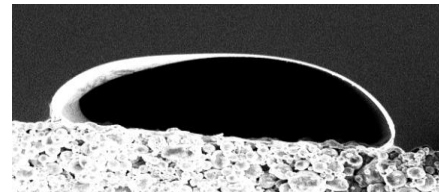
(b) AM image

Figure 18 (a) One sun open-circuit PL image zoomed into a specific region of interest within the PERC cell with numerous voids highlighted by a yellow box in Fig. 17(a). (b) AM image of the same region. Here, white channels contain voids while darker grey channels do not and represent good local back contacts. (c) SEM images of the three sites are highlighted in (a) and (b). These three sites represent the case of a good contact, a void with a BSF (less detrimental – resistive loss only), and a void without a BSF (most detrimental – resistive and recombination loss).

Following the description of the image processing technique concerned with the open-circuit image, as a future study, line-by-line comparison of two simple EL and PL images can be used to distinguish resistive only voids from the most detrimental type described here. This type of void is comprised of either a partially filled eutectic layer or no eutectic layer at all. The aforementioned void type is supposed to be present only on the EL image since it is essentially

caused by the increase in series resistance. This feature should not appear in open-circuit PL images due to it being not sensitive to resistance effects.

3.2.5 Conclusion

An algorithm, combining Fourier analysis, aimed to spatially detect the most harmful type of voids is defined. AM and SEM studies are used to validate the existence of different features (e.g. eutectic layer, BSF), which govern the physics of what is observed in PL images. This method of detection has the capability to locate the central point of voids in a manner of seconds. PL detection takes around a second and our algorithm runtime is 2 seconds. The actual physical size, known by the manufacturer, can be used to associate an area fraction affected by voids to a cell. These measurements do not require any calibration procedure and can be used in a production line as this PERC technology becomes more dominant today.

CHAPTER 4 – NOVEL CLEANING PROCEDURES

This chapter will concern with the subtleties cleaning procedures and the physical mechanisms concerned with oxidation state of the surface on which the tunneling dielectric layer will be grown. As will be shown, surface control plays a remarkable role in the passivation of crystalline silicon solar cells. Hydrophilic surfaces enabled by novel clean processes not only help maintain surface cleanliness, during the transition to another process, but also enable an extremely precise conformal growth mechanism deemed crucial for tunneling oxide layers such as aluminum oxide.

4.1 Introduction

The sole purpose of wafer cleaning procedures is to remove any particulate and/or foreign chemical elements from the surface of the semiconductor without any harm or altering surface in an undesired way. Almost all cleaning procedures evolved with the silicon semiconductor devices in mind since this technology constitutes not only the most significant portion of industry in PV but also in integrated circuits (ICs). As observed in many process steps, PV industry definitely took advantage of the prior knowledge in cleaning from the IC industry. However, due to cost restrictions enforced by the interminable price reductions in PV world, elaborate cleaning processes commonly applied in IC cannot be justified to be used in PV. Therefore, if one could come up with a solution that performs in a similar quality as obtained by RCA cleans, it would be quite appealing for PV industry. The long-established wafer cleaning approach with wet-chemical procedures has utilized hydrogen peroxide solutions in IC industry. However, these chemicals require large consumption and create problems when it comes to disposing the chemical waste,

which requires a more process friendly alternative. For this purpose, diluted hydrofluoric (HF) acid followed by a diluted hydrofluoric acid clean is adopted by PV industry. Traditionally, several wet-chemical process steps are taken in a PV-line prior to any other step. This starts with removal of any organic residues that may originate from earlier ingot-wafer processes (e.g. Czochralski process, ingot slicing) by the use of ozonated water solution. And ozone is known to be quite effective in removing organic residues, that is why high level of precautions need to be taken in production environment to make sure that ozone gas is not inhaled by someone. Saw damage removal follows this step, which usually involves alkaline etching by a potassium hydroxide (KOH) solution. As with many silicon removal steps, oxidation of the semiconductor surface requires some silicon material and this is followed by dissolution of the oxidant product. There are many wet-chemical processes utilized in a PV-line (texturing, edge-isolation, phosphosilicate glass removal), though we will only focus on cleaning in this dissertation.

4.2 Types and Origin of Contaminants

Contaminants may exist on a semiconductor surface either in the form of a film, discrete particle (or particulates), or adsorbed gas. Contaminants residing on the surface of a device can be categorized as molecular compounds, ionic materials, or atomic species. These molecular compounds can be greases, solvent residues, organic particles originating from deionized (DI) water. Cations and anions (Ionic compounds) may arise from physically adsorbed or chemical bonds of inorganic materials (sodium, fluorine, and chlorine). Metal atoms or elemental species such as gold and copper can also be observed due to solution comprised of HF or metal remains coming from an equipment. For example, even the potassium in KOH solutions, used for texturing and saw-damage removal, can penetrate into the bulk of the material and cause some lifetime

issues in high-efficiency solar cells. As will be shown later in detail, power of hydrogen (pH) control of the cleaning solution has quite a significant effect in keeping these metal impurities away from the silicon surface. Since these metal impurities and the hydrogen ions in the solutions have the same charge, there will be competing processes for adsorption onto the surface. This is also known as out-plating.

4.3 Impact of contaminants on semiconductor devices

The resulting effect of contaminants on the device performance involve number of physical phenomena and depend on the quantity and the type of the contaminant. As the thickness of PV solar cells decrease, the control on surfaces becomes increasingly important. Table below illustrates the impact of different types of contaminants [53].

Table 5. Effects of different types of contaminants.

Molecular	Ionic	Atomic
- Hinder adhesion - Form harmful decomposition products - Nucleate defects in films	- Can diffuse on surface, bulk or at interfaces - Deteriorate device performance and yield - Result in crystal defects	- Can diffuse readily - Nucleate crystal defects - Cause surface conduction

Contaminant films that are in the form of molecular compositions can inhibit the adequate cleaning and rinsing, impede proper adhesions of deposited films and is capable of forming adverse decomposition products. For instance, in the presence of non-oxidizing atmosphere at high

temperatures, organic residues may carbonize, and following the interaction with silicon substrate, and form polycrystalline regions during an epitaxial growth.

Another type of contaminant is the ionic one, that, with the application of high temperature steps or an electric field, they diffuse into the bulk or cover the surface of a semiconductor resulting in electrical imperfections. As an example, mobilized alkali ions (Na^+, K^+) that can be found in silicon oxide films give rise to undesirable surface potential, and drift currents that in essence diminish the oxide breakdown field pertaining to thermally grown silicon oxide films.

As the metal impurities present themselves in the middle of the bandgap energy levels, their contaminants are specifically detrimental for the performance of silicon devices. As the silicon resides above hydrogen when it comes to the electromotive series of elements, that signifies the order of tendency in which different chemical species may acquire or give out electrons, and is measured, in volts, with respect to an hydrogen electrode [54]. Galvanic action governs how heavy metals, especially contained in HF solutions, may out-plate onto the surface of a semiconductor. Furthermore, since most common silicon processes include high temperature steps, these metallic species can readily penetrate into the silicon substrate and create energy levels in middle of the forbidden bandgap acting as trap centers, resulting in paramount recombination levels. Additionally, they also alter the interface properties in terms of creating inversion or accumulation layers, introducing extortionate leakage currents, which essentially increase the surface recombination velocity. Table below portrays some of these impurities.

Table 6. Metallic Impurities.

Heavy Metals (most detrimental)	Alkali Metals (detrimental)	Light Elements
• Fe, Cu, Ni, Zn, Cr, Au, Hg, Ag	• Na, K, Li	• Al, Mg, Ca, C, S, Cl, F

To circumvent the detrimental outcomes of these foreign species, identifying to root cause turns out to be quite a relevant event. These measurements have to be sensitive enough to pick-up extraordinary concentrations down to 10^7 metals atoms per cm^2, which can be conducted either in-situ or separately. Secondary ion mass spectroscopy (SIMS) and total reflection x-ray fluorescence (TXRF) measurements, combined with vaper-phase decomposition methods that enable to concentrate impurities (droplets) at a specific location, significantly contributed to the achievement of this detection limit [55]. Since these impurities can diffuse quite easily, sometimes even at lower temperature ($\approx 40°C$), into the bulk material, volume-sensitive measurements are often utilized as well such as surface photovoltage (SPV) to assess minority-carrier diffusions lengths, and deep-level transient spectroscopy (DLTS) to obtain bulk lifetime.

4.4 Applications to high-efficiency solar cells

As the efficiency of solar converters approach the SQ-limit, providing clean surfaces becomes extremely crucial to enable high lifetime devices and growth of effective surface passivation layers. Traditional wet-chemical benches found in PV lines utilizes chemicals such as sulfuric acid (H_2SO_4), nitric acid (HNO_3), hydrofluoric acid (HF), hydrochloric acid (HCL), and maybe hydrogen peroxide (H_2O_2). These chemicals are subject to frequent refreshment procedures as they run through different wafers, or when a certain amount of time elapses, which is required to sustain effective cleaning of surfaces [56]. RCA cleaning can be used as a standard to judge the quality of any revolutionary cleaning step that is aimed to be introduced in a PV line since it has been shown to perform quite well in IC industry. However, since RCA cleaning requires highly concentrated chemicals and frequent renewal of the wet-benches, it is too expensive to be utilized

in a PV line. Therefore, the alternative has to be comparable to this standard and cheap at the same time. Chemical reactions below illustrate the steps governed by the RCA cleaning [53].

$$NH_4OH + H_2O_2 (30\%) + DI\ H_2O\ (at\ 70\text{-}80°C)$$

$$HCL + H_2O_2 (30\%) + DI\ H_2O\ (at\ 75\text{-}80°C)$$
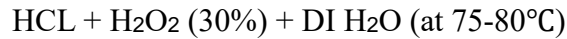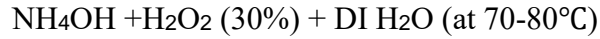
, where the initial reaction, also known as standard clean 1 (SC1) is aimed to oxidize the surface organic residues and get rid of metal ions. The second one, standard clean 2 (SC2), removes alkali cations (e.g. Na^+), main-group metals (Al^{+3}, Mg^{+2}), and transition metals (Fe^{+3}).

Dissolving ozone radicals in water has been a subject to number of studies to replace the costly RCA cleans [56, 57]. If an electrical discharge is made available around an oxygen molecule, it will split into elemental oxygen. And as these elemental species interact with the other oxygen molecule present in the surrounding volume, ozone will be formed. Figure below illustrates this phenomenon.
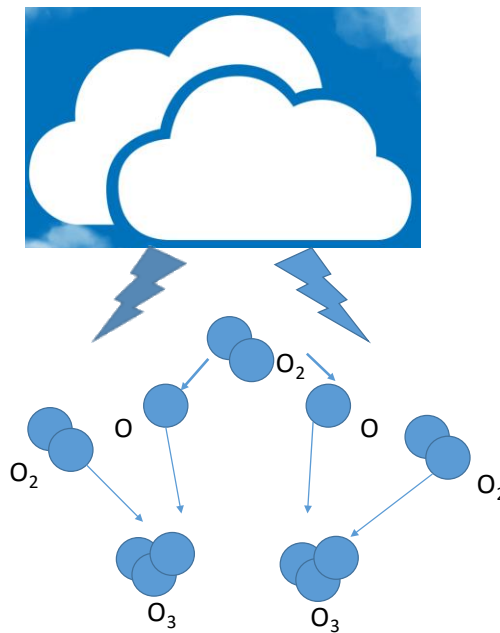

Figure 19 Ozone generation from oxygen molecules via discharge.

This generated ozone has a short half-life, which implies that it can readily relapse back into molecular oxygen. Lightning events are a prime example of ozone generation in common life scenarios, which is the reason of fresh air smell following a thunderstorm [58]. Ozone dissolved in deionized water (DIO_3) has comparable oxidation capabilities to that of hydrogen peroxide (H_2O_2). Moreover, since the surface treatment with ozonated water results in lower metal contamination on the surface than an RCA clean, the need for concentrated HCL clean is less pronounced [53]. DIO_3 containing cleans can appear in many varieties due to their versatility, though two such solutions will be subject of this dissertation. First one will mostly function to oxidize the silicon surface which is useful for many reasons as will be discussed, and this is followed by dipping in HF. The concentrations for this step are 10ppb O_3, HCL 1%, HF 1% [59]. Even though this clean is not aimed to etch the surface in substantial amounts, if repeated tens of nanometer of silicon substrate can be removed which has a number of benefits. For instance, if this clean is meant to be used following a diffusion process, extreme control in removal thickness provided by the oxidizing behavior of the clean can be exploited to tailor the peak doping density at the surface. The beauty of this oxidized surface occurs due to the fact that chemical oxidation is a self-limited process and it saturates around 1-1.2nm of thickness [60]. As observed from the last step of this cleaning, HF-last most often provides hydrophobic surfaces, which initially was believed to be caused by Fluorine termination of the surface. As the HF concentration goes down H-terminated surfaces becomes more dominant over the F-terminated ones. Fluorine terminated surfaces are believed to be responsible for the rate of native oxide growth as the wafer is exposed to air [61]. Though there have been some arguments initially, with the current understanding of HF treated surfaces, hydrogen (not the fluorine) terminated dangling bonds are the cause of hydrophobicity [53].

As highlighted many times within the flow of this work, presence of metal impurities can alter the performance of solar converters drastically, and cleaning procedures play a substantial role in this regard. These aforementioned impurities (Fe, Cu, Zn, etc.) are preferred to reside on the surface, instead of diffusing into the bulk, perhaps by means of a high temperature step, since they can be washed off of the surface via cleaning. However, certain transition metals, especially copper (Cu), can diffuse readily into the bulk material even at room temperatures, prior to any oxidation and diffusion step. Evidently, this situation dictates that cleaning solutions should preferably be free of Cu. This may not be the case especially with texturing or saw damage removal steps most commonly conducted by using potassium hydroxide (KOH) solutions. These chemical mixtures are alkaline in nature (pH$\approx$ 14), which brings the fact that out-plating of metals onto the surface of a device is quite a probable event. The control of out-plating behavior is usually provided by tweaking the HCL concentration, and altering the pH, in a given clean. In a liquid solution, HCL is completely dissolved which results in H^+, and CL^- ions in the solution. These chlorine ions play a significant role in keeping metals away from the substrate, as, given their negatively charged nature, they bind to metal ions in the solution. Moreover, chlorine ions form these aforementioned complexes with most metals, except for copper, which makes dealing with KOH solutions even more challenging. Therefore, current cleaning steps utilized in a traditional AL-BSF cell architectures with HF+HCL cleans perform poorly in cleaning Cu. Another crucial point that is affected by the presence of HCL is the oxidation of the surface, which is one key aspect of the DIO$_3$ shown before. The higher solubility of ozone is enabled by adding HCL into the solution and lowering the pH, which relates to $-\log$ [hydrogen concentration]. As more O$_3$ dissolved in the solution oxidation will be more available.

Figure below illustrates how different surface finishes look like, namely the hydrophobic and hydrophilic case.
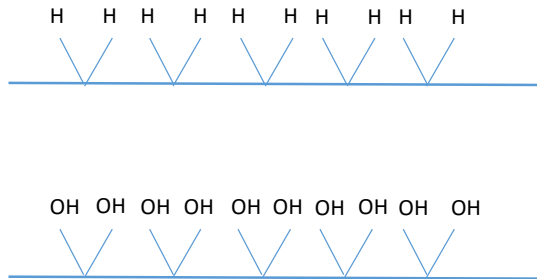
As the surface portrayed with H-terminated bonds in Fig.20 exhibit nonpolar behavior, water will be repelled owing to its polar nature. This interaction, in the hydrophobic case, also results in water droplets formed at the surface of a wafer. Hydrophobicity is created following the HF molecules attacking the Si-O bonds as they penetrate between Si and O atoms. This reaction not only occurs readily due to its exothermic nature, but also the fact that HF and Si-O bonds are both polar. Coulomb interaction also leads to annihilation of distinct bonds in a certain order which brings the conclusion that hydrogen, not the fluorine, is what saturates the dangling bonds following an HF treatment [53]. Due to all these reasons explained, HF attack and dissociates oxides quite easily and leaving the silicon substrate unaltered.

H-terminated surfaces lead to unstable oxidizing conditions, and oxide-terminated (OH-terminated) counterparts are superior in this regard and is the reason why vendors ship wafers in hydrophilic state, usually. As will be explored with the support of experimental data in Chapter 5, hydrophilic surfaces present further paramount advantages over the H-terminated especially when

they are aimed to be used in a combination with tunneling passivation layers. Figure below portrays the principles that underlie the reasoning to how metal can be repelled from the surfaces of a wafer.
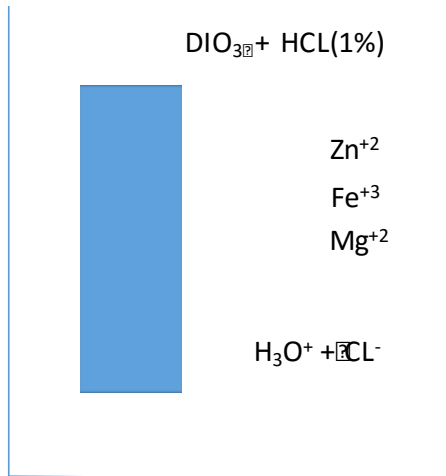
Figure 21 Control of metal impurities via the use of HCL.

As the hydrochloric acid dissociates readily in the solution to H_3O^+ and Cl^-, positively charged ions "compete" with the metal ions as they race to the surface, and also chlorine ions are interacting heavily with many of those metals to form complexes.

The other type of clean that incorporates DIO_3 solution is the mixture of HF+HCL, which demonstrates both oxidizing and reducing species simultaneously [56]. This mixture also comes with the more pronounced etching nature than the ones that only have HCL, as expected. Up to this point, it has emphasized many times that lower pH values (high concentration of HCL) are favorable for many reasons. However, the interaction between chlorine ions and the ozone is what puts a boundary on this phenomenon, yielding an interesting tradeoff between these two species as shown by figure below.
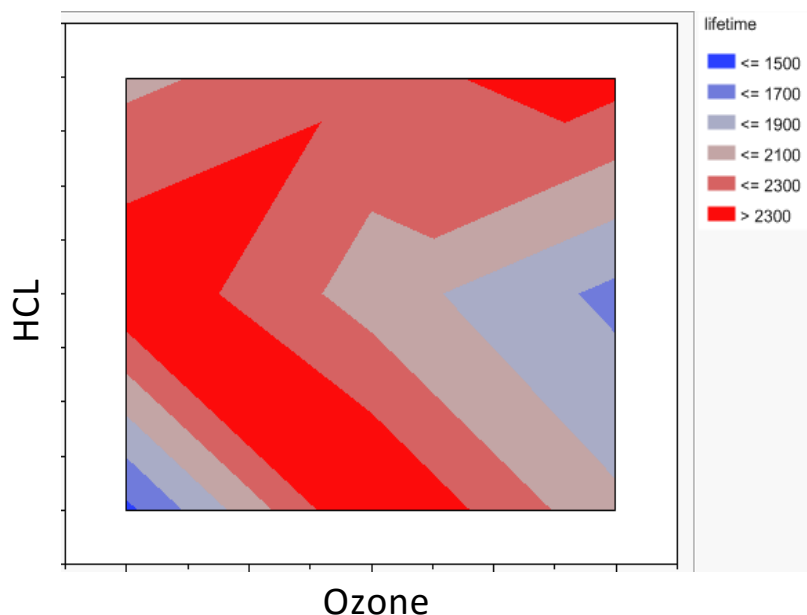
Figure 22 Chlorine and Ozone interaction. Lifetime values are in microseconds.

What Figure 22 shows is that higher HCL concentrations, lower pH values, is required to dissolve more and more ozone into the solution. However, as chlorine ions becomes more available in the solution, then these species will start interacting with ozone molecules, the creation of which were facilitated by the chlorine ions themselves. Chlorine behaves as a catalyst in breaking down reaction of ozone that eventually frees up an oxygen atom and two oxygen molecules. This trade-off between HCL and ozone dissolution is what is portrayed by the mid HCL levels in the Figure 22. Units are not shown because of confidentiality reasons. This exact phenomenon is also observed in the atmosphere. Stratosphere is where most of the ozone on earth resides between an altitude of 6 miles to 31 miles above surface. This is the layer that enables the absorption of many harmful ultraviolet rays. As the CFC molecules (chlorine, fluorine, carbon) reach to the stratosphere, due to their exceptionally high lifetimes, they will interact with high energy photons, individual chlorine components will act as catalysts, just like in the cleaning procedures described

above, to steal an oxygen from the ozone so that it will be broken down into two oxygen molecules. This chemical reaction that describes the depletion of ozone is shown below [62].

$$Cl + O_3 \rightarrow ClO + O_2$$

$$ClO + O \rightarrow Cl + O_2$$

$$O_3 + O \rightarrow 2O_2$$
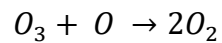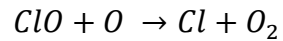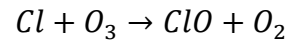
4.5 Conclusion

Results obtained due to the understanding of this chemical interaction, as shown in Figure 22, help optimize the process window where certain cleans can be most beneficial. This becomes specifically important when oxidizing and the reducing species coexist in a given clean tank. The introduction of industrially relevant cleaning procedures is deemed instrumental especially as the current cell architectures become more efficient, where even a minute impurity concentration can destroy device performance.

CHAPTER 5 – SURFACE PASSIVATION

5.1 Introduction

As the efficiency of crystalline silicon solar cells approaches its intrinsic limit, some sort of passivation scheme within the contact where the extraction of carriers occur becomes essential. This stems from the fact that there exists high a density of recombination centers where the metal touches the silicon. Historically, this problem was dealt in two ways. First introducing a heavily doped region right underneath the contact where the metal-silicon interface takes place (e.g., selective emitter, selective back surface field). However, this introduces complexity in manufacturing due to patterning and alignment requirements, it increases Auger recombination, and ultimately does not achieve the saturation current densities needed to push cells beyond 25%. This limit is closer to around 22% using industrial processes (e.g., screen-printing) [41]. The second approach is limiting these metal-semiconductor interfaces to a smaller fraction of the interface. Therefore, carriers will have to travel laterally to the contacts where the extraction takes places (i.e., three-dimensional carrier transport). This brings the trade-off between the fill-factor and the open-circuit voltage of the cell. Moreover, this scenario also necessitates the use of highly-doped substrates because of resistance problems, which will increase the bulk recombination. A transition is currently taking place in industry from aluminum back surface field (Al-BSF) cells to passivated emitter rear contact (PERC) cells is a prime example of such a phenomenon.

Another approach to the problem is the use of heterostructures to provide contact passivation. This can be done by using a homojunction and tunneling passivational layer, as in a metal-insulator-semiconductor (MIS) structure [63], or by using carrier selective heterojunctions, like amorphous or polycrystalline silicon [64]. Recently there has been a tremendous interest in

metal oxide materials for the passivation of the metal-silicon interface. Molybdenum oxide [65], and titanium oxide [66] have been demonstrated in hole and electron extraction layers, respectively. While these somewhat exotic materials have shown promise, being able to achieve the same passivation and carrier extraction properties with a material already in use by industry would likely lead to more rapid adoption by the industry.

Aluminum oxide (Al_2O_3) is an established passivation layer in the solar industry, offering exceptionally high negative built-in charge for field effect passivation of p-type surfaces while offering a fairly low interface defect density [67]. Because of these properties, it has been combined with silicon nitride by many research groups and industry to form an insulating passivation stack for p and p^+ surfaces (e.g., rear side of PERC cells, front side of n-type cells). Therefore, adoption of Al_2O_3 in a metal-insulator-semiconductor contact may bring many advantages. However, this insulating layer has to be thin enough such that there is a high probability for tunneling. This requirement also brings the challenge of growing thin films conformally with low thickness variation such that high passivation quality is maintained over the entire surface of the wafer. Traditionally, the removal of any possible silicon oxide layer is done prior to the deposition of Al_2O_3, typically with hydrofluric (HF) acid. However, as it is shown by previous research groups [68], if these films are deposited on non-OH-terminated surfaces (i.e., HF-last), formation of island-like shapes take place on the surface, prohibiting the conformal growth of the film. This is exteremely crucial in a structure like crystalline-silicon solar cell, which is a fairly large area device.

In this dissertation, we investigate the use of an SiO_x/Al_2O_3 stack as a hole selective, tunneling contact on p^+ surfaces with a $\approx$113 $\Omega/\square$ sheet resistance formed using a BBr_3 diffusion.

This structure can be applied to both *p*-type cells, as a BSF, or *n*-type cells, for emitter passivation (Figure 23).
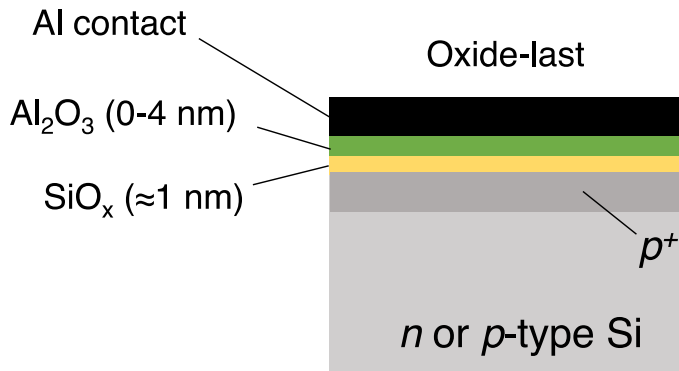
Figure 23 Proposed structure for the conformal growth of tunneling layers.

5.2 Atomic Layer Deposition of Aluminum Oxide

As the layer thickness reaches levels of tunneling dimensions, control over the stoichiometry, surface topology, and conformality becomes highly important. As shown by earlier work, only atomic layer deposition technique can achieve the desired surface conformality on structures with high fidelity [69]. These crucial properties are enabled inherently owing to the nature of the deposition, which is provided by serial and self-limiting surface reactions. Precursors enter the reaction chamber one at a time and the reaction with the substrate takes place sequentially and in a self-limiting manner. What this implies is that the reaction between the surface groups and the gas-precursors is naturally terminated since available surface group will be saturated for a pumped reactant at a given pump cycle. Common ALD processes utilize two gas precursors (e.g. trimethylaluminium (TMA) and water) and these react with surface groups in an alternating manner. A given precursor (TMA) reacts with the available, unsaturated, surface group and this will lead to volatile reacting species that are pumped away from the chamber, and the second

precursor (water) is introduced. Within the flow of these reactions, first the surface group rejuvenates to enable the deposition of the next set of atomic layers, and the second layer is deposited [67, 70]. ALD is distinguished from chemical vapor deposition (CVD) in the sense that precursors are introduced at different times (separately) and this brings the advantage of deposition rate not being proportional to precursor flux. As the substrate is subject to reactants in an individual fashion, the resultant film is formed in a stepwise manner. This makes the ALD deposition process almost ideal for non-planar surfaces so that conformal and pinhole free films can cover the whole available area.

The most prevalent precursors used to deposit aluminum oxide by means of ALD are trimethylaluminum as a source of aluminum and water as a source of oxygen. Oxygen can also be introduced from ozone sources as well. ALD processes can be in the form of either thermal or plasma-assisted, where the latter provides higher energies for reaction to start. This availability of initial energy provides increased film quality which is crucial to grow film on substrates that have low temperature requirements. Furthermore, common to all ALD processes, which mainly distinguishes it from CVD, is the purging of the first precursor, TMA, is separated from the secondary source via purging. ALD may also present some challenges in terms of not being able to grow every material and precursor problems. However, these can be mitigated for the sake of solar cell purposes [67]. The requirements for precursors to be utilized in ALD processes are (1) Volatility (vapor pressure $> 0.1\ Torr\ at\ T < 200\square$), (2) having the ability to react with the substrate in a self-limiting manner, (3) no thermal decomposition (4) the resulting byproducts is not supposed to etch the film, or alter the surface groups.

As the available water vapor in atmosphere, ALD being a non-vacuum process, is subject to adsorption by the surface of the semiconductor, a hydroxyl group is likely to be formed, Si-O-

H. To initiate the very first set of reactions, TMA precursor is pumped into the reactor to interact with the aforementioned hydroxyl group [71].
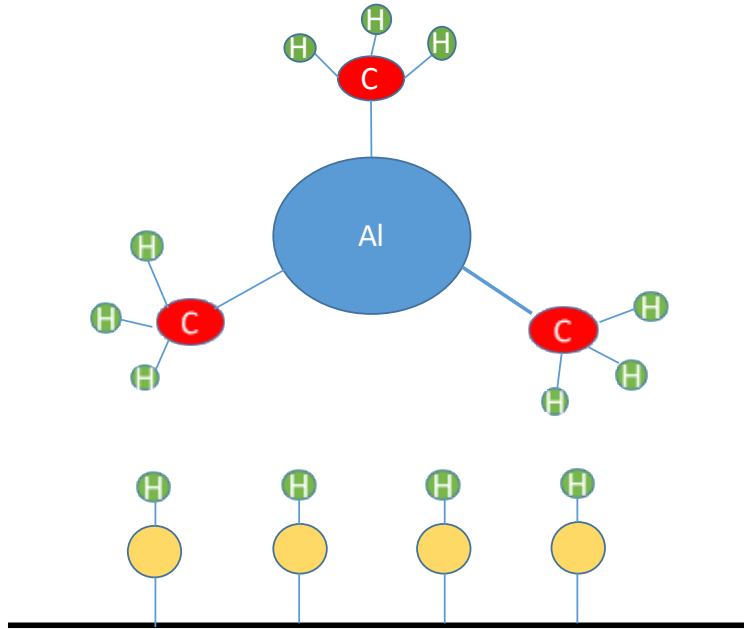
Figure 24 The structure of chemical bonds prior to interaction of TMA precursor.

Figure above illustrates how the available chemical bonds present themselves prior to interaction of the TMA precursor with the surface groups. Following this event, TMA precursor saturates the hydroxyl groups, leaving methane gas (CH_4) byproduct that is pumped away with the excess TMA. Furthermore, water precursor is introduced into the chamber as a source of oxygen to interact with the dangling methyl groups on the surface. This reaction, with the methane byproduct, will lead to Al-O species and hydroxyl (OH) seeking TMA pulse to be saturated. While this process, due to its self-limiting nature, creates almost ideal passivation schemes, the key requirement is that precursors should not react with themselves. These aforesaid cycles lead to aluminum oxide mono-layers with thicknesses of 0.9-1.5nm [67].
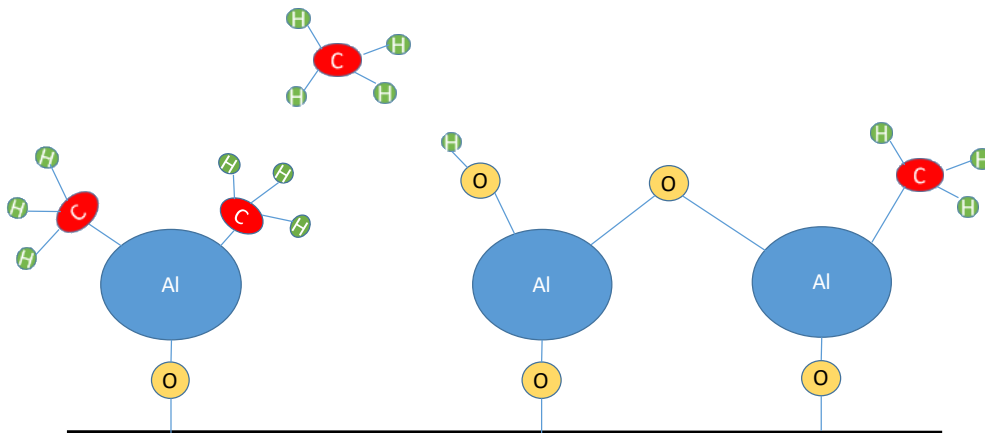
Figure 25 Chemical structure of the species after water precursor interaction.

Figure 25 portrays the chemical bonding following the water precursor interacting with the dangling methyl group, with the first monolayer formation of aluminum oxide. Chemical reactions associated with these two cycles are shown below with the methane byproduct.

$$Al(CH_3)_3 + Si - O - H \rightarrow Si - O - Al(CH_3)_2 + CH_4$$

$$2H_2O + Si - O - Al(CH_3)_2 \rightarrow Si - O - Al(OH)_2 + 2CH_4$$
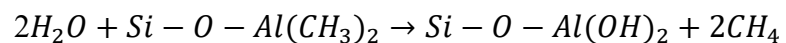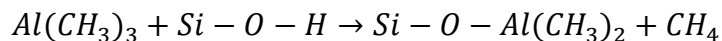
Between each of these reactions, the products will be pumped away, and surface groups will be made available for the upcoming precursor. The importance of how the hydroxyl group is supplied will be discussed later in this chapter as this constitutes a major message for this dissertation.

5.3 Surface Passivation Properties of Tunneling Aluminum Oxide Films

As crystalline silicon solar cells usually have large surface areas (6" by 6"), for real products, providing spatially uniform passivation layers is a non-trivial task. This uniformity issue also appears in nanoscale where first monolayers are formed during ALD deposition. Traditionally, before any deposition of a passivation stack, the surface of crystalline silicon wafers is subject to hydrofluoric acid treatments to remove any possible oxides, and as shown earlier in chapter 4, this leads to dominant H-terminated surfaces. These surface chemistries are, to describe it even more precisely, in the bonding structure of CH_3 bonded to single atomic monolayers of aluminum as portrayed precisely in Figure 25 [68]. An alternative way to continue the cell process, which can be of interest, is the preparation of OH-terminated surfaces, that can be prepared easily by deposition of chemical oxide. As high-k dielectrics have been studied intensely on integrated circuit (IC) industry, adopting the already existing knowledge into the current solar cell architectures would prove to be handy solution. To be able to reason the possible benefits of utilizing such a surface finish requires the use of sophisticated surface characterization approaches. Chief among which are named as atomic force microscopy (AFM), and water contact angle measurements, that are aimed to be complementary to lifetime and other electrical measurement techniques. Contact angle measurements provide insight, with a quantitative sense, into wettability of a given surface, that is a solid, as governed by Young equation [72]. As shown in earlier work [68], as the aluminum oxide thickness increases the contact angle for a hydrophobic (H-terminated) surface decreased monotonically. Most often, surface structures manifest linear relationship between water contact angle and surface roughness as will be proven by AFM measurements later on. This indicates that growth instability can be triggered by rougher surfaces

forming higher water contact angles for processes that corporate water as a source of oxygen in ALD [68]. On the other hand, the OH-terminated surface exhibits a fixed water contact angle, as the deposited film thickness increases. To be able to ascribe this physical behavior to surface roughness quantitatively, AFM measurements are used, which will not only portray how the layer evolve as a function of thickness but also provide root-mean-square roughness value.
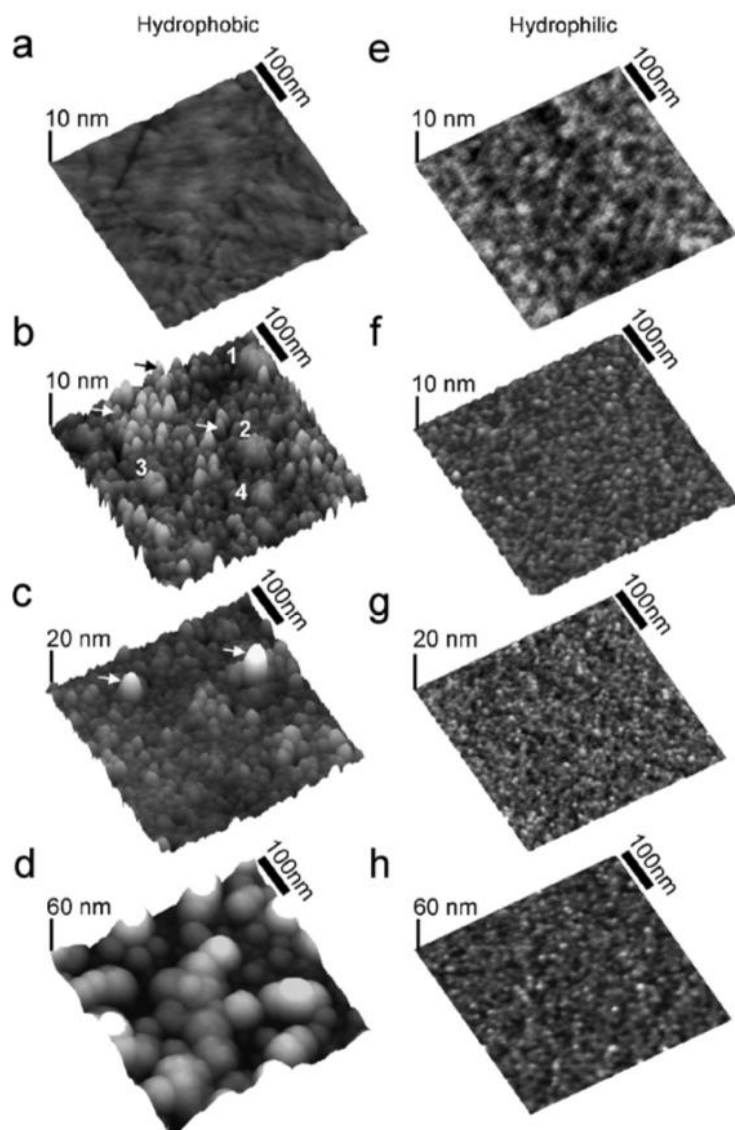

Figure 26 Non-contact AFM images of aluminum oxide layers on H-terminated (a-d) and OH-terminated (e-h) surfaces with different number of ALD cycles (0, 100, 200, 400).

Table 7. Comparison of surface roughness for H-terminated (CH3-SAM) and OH-terminated surfaces for different number of ALD cycles.

Surface finish	ALD cycle number	Thickness (nm)	RMS roughness (nm)
CH3-SAM	100	8.2	1.23
	200	17.6	2.16
	400	39.2	8.09
OH-SiO2	100	10.6	0.24
	200	20.3	0.27
	400	35.9	0.37

As depicted in Figure 26 pictorially and quantified by the root-mean-square surface roughness values, one could clearly conclude that hydrophilic (OH-terminated) surfaces provide a much smoother growth mechanism compared to hydrophobic (H-terminated) ones [68]. The physical reasoning for this behavior to take place can be explained by the fact that with the surfaces that have CH3 termination, the precursor, TMA, will react in a spontaneous fashion with the surface groups (water droplets) that formed as a result of the water vapor in the chamber. This situation reflects on the growth stability problem in the form of dome-like structures. These island-like shapes will start to smooth out as the thickness grows, but their impact on surface morphology is quite detrimental for thin layers (<5nm). Therefore, in the light of these surface studies one could conclude that surface wettability has quite a significant impact on the reaction between the precursors used in the ALD, and proper control of surface groups must be maintained so that atomically smooth morphologies can be obtained especially for tunneling regime which lies in the heart of this dissertation.

To circumvent this phenomenon of non-conformal growth, our group studied the deposition of very thin layers of Al_2O_3 (1-3nm) on hydrophilic surfaces. We wanted to observe if the same physical principles apply to a batch ALD process which can be used for a PV-line where 3600 wafers per hour are processed. For this purpose, each building block of this passivation stack is thoroughly examined. As an initial step, a chemical oxide deposition study took place. Mirror-polished CMOS wafers were used for optimized ellipsometry measurements. All samples were initially dipped in a mixture of ≈1% HF, stripping any surface oxide and ensuring that the initial condition of the surface was hydrophobic. Following this, samples were immersed in a chemical bath where ozonated dionized water mixture exists. The variation of the chemical oxide thickness was studied as a function of immersion time. Importantly, since this is a large- area device, uniformity of this chemical oxide was quite crucial. This was verified by 49-point ellipsometry measurements.

Table 8. Chemical oxide thickness from 49-point ellipsometry measurements for the solar cell line process.

	0 sec.	10 sec.	25 sec.	45 sec.	60 sec.	90 sec.
Mean (nm)	0.120	0.819	0.882	0.946	0.951	0.950
St. Dev. (nm)	0.016	0.014	0.009	0.01	0.011	0.014

As can be seen from table 7, hydrophilic surface finish provides exceptionally uniform films, as validated by ellipsometry measurements. To judge how the film evolves as a function of thickness, we wanted to compare our batch ALD process to a well-developed CMOS tool which utilizes a temporal ALD instead of a spatial one.

What is depicted in Fig. 27. is the extreme similarity in oxide growth process between a CMOS tool and a solar cell R&D tool. The CMOS tool follows the following process: (HF(2%) DIW/O_3 DIW Drying in N_2). The solar cell tool, on the other hand, includes the following steps: (HF(2%) DIW DIW/O_3 Drying in N_2). As one can see from Table 7, the standard deviation in 49-point ellipsometry measurements is extremely low.

After confirming that conformal growth of this chemical oxide was highly stable, our group went on the investigation of the second dielectric layer in this stack, Al_2O_3. Before we illustrate the findings of this experiment, the theory of why Al_2O_3 is the material of choice will be the subject of the next sub-chapter.

5.3.1 Experimental Findings

Symmetrical lifetime structures were created as a part of this dissertation. Any problems with the growth mechanism will cause a decrease in lifetime. Below graph illustrates the evolution

of emitter recombination current density as a function of Al_2O_3 thickness deposited by spatial atomic layer deposition (ALD).
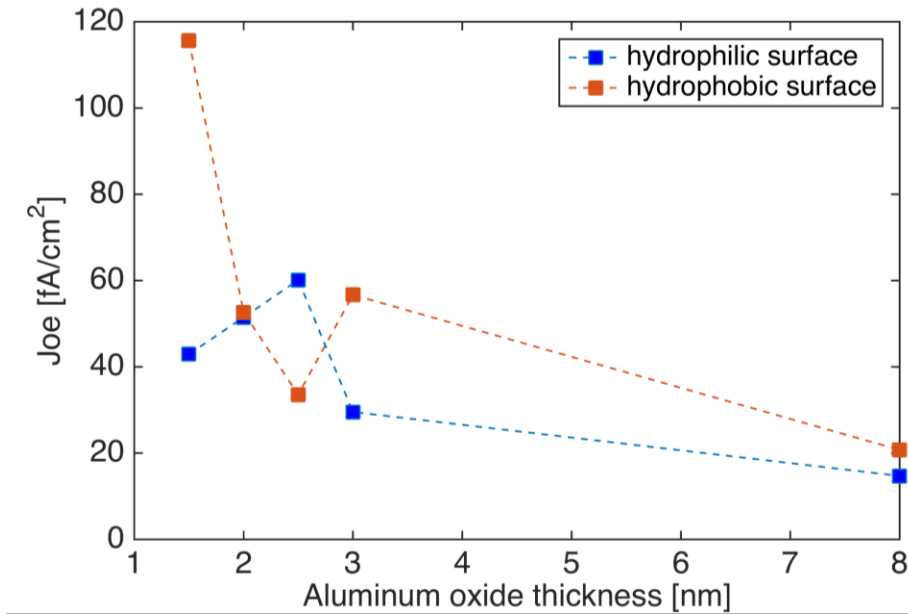
Figure 28 Evolution of emitter saturation current density (Joe) vs. Al2O3 thickness.

The spatial ALD tool from SoLayTec is utilized for this study with a deposition temperature of 200℃ with precursors trimethylaluminum (TMA) and water vapor. The emitter recombination current density (J_{oe}) values are extracted via using the well-known Kane and Swanson method from carrier lifetime mesurements with the aid of Sinton coil [73]. Intrinsic carrier density is assumed to be $9.70 \cdot 10^9 cm^{-3}$ at 300°K.

As can be seen, for the first time, J_{oe} values on the order of 40fA/cm^2 were demonstrated with an Al₂O₃ layer that is 1.5nm thick. This is, to our knowledge, the best passivation and carrier extraction quality obtained with tunnelling Al₂O₃ layer. The key message, though, is the three-fold difference, in recombination factor, between the hydrophobic and hydrophilic case for 1.5nm of

Al₂O₃. This is solely due to non-conformal growth of the film for extremely thin layers, which is verified by other experiments.

Given that this layer must also serve as a carrier extraction path while passivating the region of interest, low contact resistivity values are also quite essential. To investigate this, transfer length method (TLM) test structures were created by using thermal evaporation of aluminum. These aluminum stripes were 200nm thick, deposited using a shadow mask. In our experience, these TLM measurements were quite repetable perhaps due to the high uniformity of the process developed.

TLM method has been used quite ubiquitously in the literature before since it provides access to contact resistance, ρ_c, information in a very simple manner, which is theoretically defined to be the derivative of the current density with respect to voltage around the voltage point being equal to zero [74]. Common electrical measurements are not capable of accessing ρ_c directly, thus contact resistance (Ω) is further interpreted utilizing additional methods to obtain the contact resistivity ($\Omega.cm^2$), ρ_c. Test structures need to be prepared for TLM measurements and these are shown in the figure below [75].
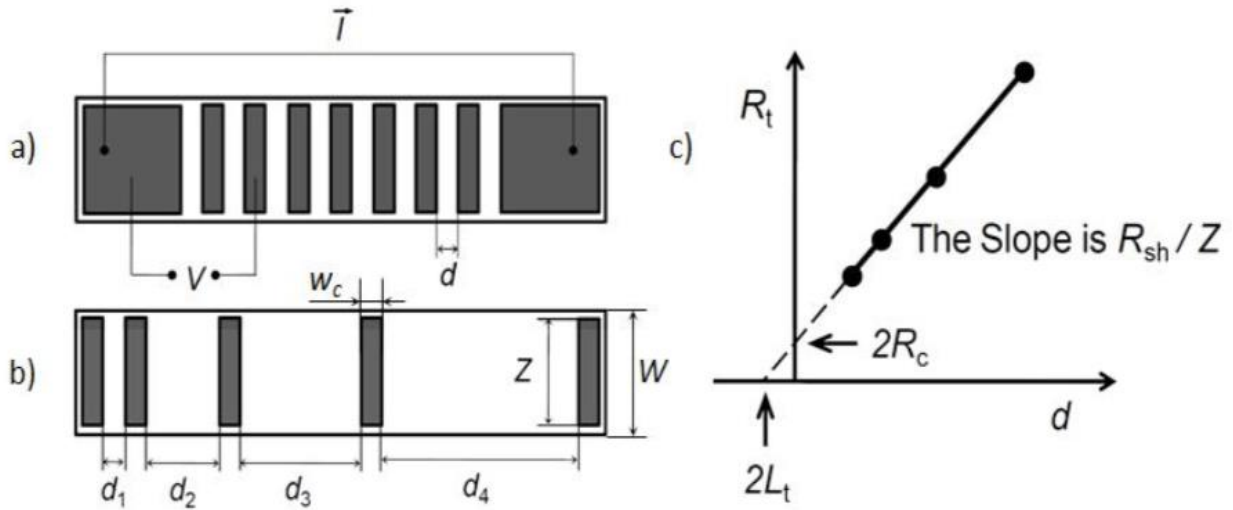
Figure 29 Contacts as observed from the top surface of the test structures (a) and with unequal spacings. Total resistance as a function of the contact spacing (c).

The benefit of using structures with different spacing between metal contacts is that as the voltage drop being measured, data associated with adjacent contacts cannot interfere with each other. As current flows from the emitter towards to contacts laterally, the distance at which the current diminishes to 1/e of its starting value is reported as the transfer length, L_t, which is determined by the following relationship.

$$L_t = \sqrt{\rho_c \cdot R_{sh}} \tag{27}$$

, where R_{sh} denotes the sheet resistance, and the total resistance is written as follows,

$$R_t = R_{sh}d + 2R_c \approx \frac{R_{s\boxtimes}}{z}(d + 2L_t) \tag{28}$$

As the total resistance is plotted as a function of numerous contact spacing, d, the knowledge from the equation 28 can be used to obtain three significant variables. Contact length

leads to the information about sheet resistance which essentially comes from the slope of the line in Figure 29 (c). The y-intercept of Figure 29, $2R_c$, provides knowledge about the contact resistance with the x-intercept leading to $2L_t$ and from equation 27, contact resistivity, ρ_c, is determined.
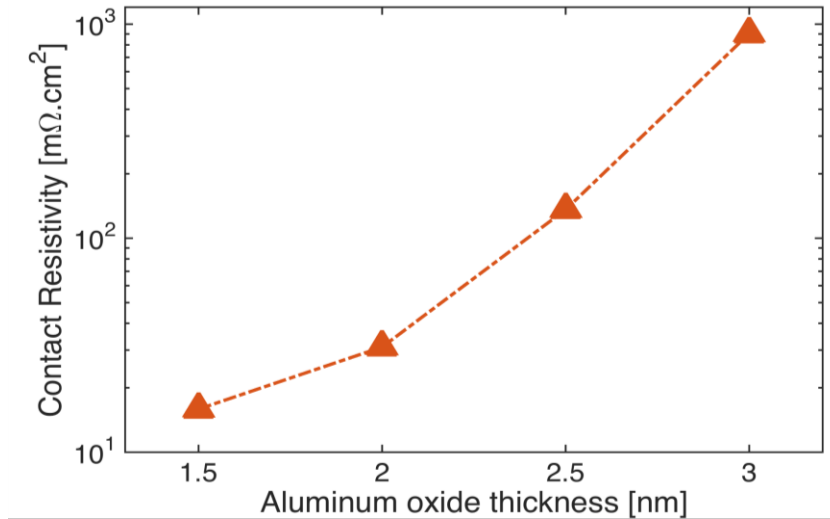
Figure 30 Contact resistivity obtained from TLM measurements.

This exponential-like growth, as illustrated in Figure 30, in contact resistivity for increased Al_2O_3 thickness is expected due to tunneling behavior. If 1D carrier transport is available, one could allow contact resistivity on the order of 100mΩ·cm^2, which was achieved with a 2.5nm of Al_2O_3 in combination with a 0.95nm thick chemical oxide. Quite interestingly, the best passivation quality was achieved with the group consisting of 1.5nm Al_2O_3 and the same chemical oxide. At this thickness contact resistivity is around 15mΩ.cm^2, which means that this stack could also be a candidate for local contacts in event that the J_{oe} is not low enough.

CHAPTER 6 – CONCLUSION AND FUTURE OUTLOOK

This dissertation has contributed to the field of photovoltaics in a number of different topics, mainly in characterization and processing. From the characterization side of the world, it initially provides a detailed analysis of previously published methods and most importantly portrays what improvements can be done to further increase the fidelity of the calculations. This opens up significant opportunities in terms of determining physically relevant important features of a solar converter in a spatially resolved manner. This was achieved via the introduction of the spatially resolved ideality factor into previously published models. Aforesaid improvements mainly refer to the capability of distinguishing different concurring loss mechanisms within the volume of the device, which essentially is enabled by avoiding the use of global ideality factor, and rather adopting the spatially resolved one. As proved by local series resistance, dark saturation values, and histograms a more effective and accurate way of calculating efficiency in a spatially resolved way is achieved. These algorithms can be applied in a manufacturing environment to see the subtleties of any processing imperfection and take precautions in seconds. To further investigate the applications of this method, we are planning on integrating the spatially knowledge of the short-circuit current density maps to gain insight into even more accurate efficiency maps.

To elucidate the importance of metrology even further, image processing algorithms that are capable of picking up void features in PERC cells are developed. This method is highly promising as it delivers an automated way of delineating what might have gone wrong in the production of this cell architecture which is shown to gain a significant market share in the near future. What this part of this dissertation contributed primarily is the use of photoluminescence imaging combined with Fourier filtering of undesired features. The resulting binary image which

is aimed to illustrate the most detrimental type of voids is further broken down into more sophisticated analysis like SEM and SAM to really pinpoint the physical root cause of the defect. This scrutiny is adopted since it validates what is really portrayed with the output images of the algorithms developed within the scope of this dissertation.

In the final part of this dissertation, an alternative way of utilizing a very well-known oxide layer, aluminum oxide, is presented as a tunneling passivation stack. This layer is chosen since its well-established physical properties as a hole passivating dielectric is promising even when the tunneling regime prevails. Record passivation (~35 fA/cm^2) and carrier extraction capabilities (15mΩ.cm^2) can pave the way for this type of stack to be used in passivated contact cells. Aluminum oxide is appealing also from the stand point of providing improvements in terms of long wavelength reflection which is crucial as this layer is proposed to be used at the back contact. Furthermore, the likelihood of having a charge located near the interface, within a couple of nanometers, enables to use of such layer for textured surfaces which is shown to be a shortcoming for other types of passivated contact stacks. The key contribution of this section is that atomic layer deposition of aluminum oxide layers on hydrophilic surfaces, enabled by industrially relevant processes, provides record passivation quality as a hole collecting layer. Most importantly, all of these processes are done on Czochralski-grown wafers with high possibility of adoption by current industrial setups.

REFERENCES

[1] M. Schmela, Global Market Outlook For Solar Power / 2016-2020., in: SolarPower Europe, 2016.

[2] R. Gray, The biggest energy challenges facing humanity

http://www.bbc.com/future/story/20170313-the-biggest-energy-challenges-facing-humanity, in, 2017.

[3] K. Crumbley, 7 Important Uses for Crude Oil and Why It Matters

https://www.biblemoneymatters.com/7-important-uses-for-crude-oil-and-why-it-matters/, in.

[4] C. Stuart, Energy and Climate Change Adaptation in Developing Countries, in, European Union Energy Initiative Partnership Dialogue Facility (EUEI PDF), 2017.

[5] S. Kurtz, H. Atwater, A. Rockett, T. Buonassisi, C. Honsberg, J. Benner, Solar research not finished, Nature Photonics, 10 (2016) 141.

[6] Terrestrial abundance of elements, in, 2007.

[7] M. Morita, T. Ohmi, E. Hasegawa, M. Kawakami, M. Ohwada, Growth of native oxide on a silicon surface, Journal of Applied Physics, 68 (1990) 1272-1281.

[8] M.A. Green, Self-consistent optical parameters of intrinsic silicon at 300K including temperature coefficients, Solar Energy Materials and Solar Cells, 92 (2008) 1305-1310.

[9] E. Yablonovitch, Statistical ray optics, J. Opt. Soc. Am., 72 (1982) 899-907.

[10] T. Kirchartz, Generalized detailed balance theory

of solar cells, Forschungszentrum Julich, 2009.

[11] W. Shockley, H.J. Queisser, Detailed Balance Limit of Efficiency of p- n Junction Solar Cells, Journal of Applied Physics, 32 (1961) 510-519.

[12] A.P. Kirk, M.V. Fischetti, Fundamental limitations of hot-carrier solar cells, Physical Review B, 86 (2012) 165206.

[13] R.T. Ross, A.J. Nozik, Efficiency of hot- carrier solar energy converters, Journal of Applied Physics, 53 (1982) 3813-3818.

[14] PVEducation: http://www.pveducation.org/, in.

[15] T. Tiedje, E. Yablonovitch, G.D. Cody, B.G. Brooks, Limiting efficiency of silicon solar cells, IEEE Transactions on Electron Devices, 31 (1984) 711-716.

[16] A. Belghachi, Theoretical Calculation of the Efficiency Limit for Solar Cells, Solar Cells - New Approaches and Reviews, InTech, (2015).

[17] U. Rau, Reciprocity relation between photovoltaic quantum efficiency and electroluminescent emission of solar cells, Physical Review B, 76 (2007) 085303.

[18] K. Yoshikawa, H. Kawasaki, W. Yoshida, T. Irie, K. Konishi, K. Nakano, T. Uto, D. Adachi, M. Kanematsu, H. Uzu, K. Yamamoto, Silicon heterojunction solar cell with interdigitated back contacts for a photoconversion efficiency over 26%, Nature Energy, 2 (2017) 17032.

[19] V.I. Fistul, Impurities in Semiconductors : Solubility, Migration, and Interactions, CRC Press, 2004.

[20] A.G. Aberle, Crystalline silicon solar cells : Advanced Ssurface Passivation and Analysis, Centre for Photovoltaic Engineering, University of New South Wales, Sydney NSW 2052, Australia, 1999.

[21] C.-T. Sah, Fundamentals of Solid-State Electronics, World Scientific Publishing, 1991.

[22] W. Shockley, W.T. Read, Statistics of the Recombinations of Holes and Electrons, Physical Review, 87 (1952) 835-842.

[23] R.N. Hall, Electron-Hole Recombination in Germanium, Physical Review, 87 (1952) 387-387.

[24] J. Nelson, The Physics of Solar Cells, Imperial College Press, 57 Shelton Street Covent Garden London, 2013.

[25] L.E. Black, T. Allen, K.R. McIntosh, A. Cuevas, Effect of boron concentration on recombination at the p-Si–Al2O3 interface, Journal of Applied Physics, 115 (2014) 093707.

[26] A. Morato, Electrical Characterization Of Thin Film Passivation Layers For P-Type Silicon Solar Cells, in, University Degli Studi di Padova, Padova, 2012.

[27] A. Cuevas, The Recombination Parameter J0, Energy Procedia, 55 (2014) 53-62.

[28] K. Öğütman, K.O. Davis, E. Schneller, V. Yelundur, W.V. Schoenfeld, Integration of spatially resolved ideality factor into local cell efficiency analysis with photoluminescence, Solar Energy, 158 (2017) 869-874.

[29] T. Trupke, E. Pink, R.A. Bardos, M.D. Abbott, Spatially resolved series resistance of silicon solar cells obtained from luminescence imaging, Applied Physics Letters, 90 (2007) 093506.

[30] M. Glatthaar, J. Haunschild, R. Zeidler, M. Demant, J. Greulich, B. Michl, W. Warta, S. Rein, R. Preu, Evaluating luminescence based voltage images of silicon solar cells, Journal of Applied Physics, 108 (2010) 014501.

[31] C. Shen, M.A. Green, O. Breitenstein, T. Trupke, M. Zhang, H. Kampwerth, Improved local efficiency imaging via photoluminescence for silicon solar cells, Solar Energy Materials and Solar Cells, 123 (2014) 41-46.

[32] Z. Hameiri, P. Chaturvedi, K.R. McIntosh, Imaging the local ideality factor by contactless photoluminescence measurement, Applied Physics Letters, 103 (2013) 023501.

[33] K. Ogutman, K.O. Davis, E. Schneller, V. Yelundur, W.V. Schoenfeld, A thorough way of mapping efficiency with photoluminescence, in: Photovoltaic Specialist Conference (PVSC), 2015 IEEE 42nd, 2015, pp. 1-4.

[34] H. Höffler, H. Al-Mohtaseb, J. Haunschild, B. Michl, M. Kasemann, Voltage calibration of luminescence images of silicon solar cells, Journal of Applied Physics, 115 (2014) 034508.

[35] S.C. Baker-Finch, K.R. McIntosh, M.L. Terry, Isotextured Silicon Solar Cell Analysis and Modeling 1: Optics, Photovoltaics, IEEE Journal of, 2 (2012) 457-464.

[36] K.R. McIntosh, Lumps, humps and bumps: Three detrimental effects in the current-voltage curve of silicon solar cells, (2001 Available:

http://handle.unsw.edu.au/1959.4/54714).

[37] C. Shen, H. Kampwerth, M.A. Green, Photoluminescence based open circuit voltage and effective lifetime images re-interpretation for solar cells: The influence of horizontal balancing currents, Solar Energy Materials and Solar Cells, 130 (2014) 393-396.

[38] H. Höffler, O. Breitenstein, J. Haunschild, Short-Circuit Current Density Imaging Via PL Image Evaluation Based on Implied Voltage Distribution, IEEE Journal of Photovoltaics, 5 (2015) 613-618.

[39] K. Öğütman, K.O. Davis, H. Ali, S.R. Martell, W.V. Schoenfeld, Automated detection of rear contact voids in perc cells with photoluminescence imaging, Solar Energy Materials and Solar Cells, 179 (2018) 31-35.

[40] A.U.D. Castro, Advanced Rear-Side Contact Schemes on i-PERC (industrial Passivated Emitter and Rear Cell) solar cells, (2013).

[41] P.P. Altermatt, K.R. McIntosh, A Roadmap for PERC Cell Efficiency towards 22%, Focused on Technology-related Constraints, Energy Procedia, 55 (2014) 17-21.

[42] M.A.T. Lenio, J. Howard, D. Lu, F. Jentschke, Y. Augarten, A. Lennon, S.R. Wenham, Series Resistance Analysis of Passivated Emitter Rear Contact Cells Patterned Using Inkjet Printing, Advances in Materials Science and Engineering, 2012 (2012) 8.

[43] E.a.U. Davanzo, Aluminum-Silicon Contact Formation Through Narrow Dielectric Openings: Application To Industrial High Efficiency Rear Passivated Solar Cells, (2012).

[44] C. Yifeng, P.P. Altermatt, D. Jianwen, Z. Shu, L. Jiajing, C. Daming, D. Weiwei, J. Yuling, L. Binhui, X. Wenming, Z. Huijun, C. Hui, J. Haijun, P. Xiujuan, Z. Ming, W. Dianlei, S. Jian, Z. Yingbin, S. Hui, F. Zhiqiang, P.J. Verlinden, Al-alloyed local contacts for industrial PERC cells by local printing, in: Photovoltaic Specialist Conference (PVSC), 2014 IEEE 40th, 2014, pp. 3322-3325.

[45] K. Dressler, M. Kratt, P.A. Voss, S. Ebert, A. Herguth, G. Hahn, Influence of Al Particle Size and Firing Profile on Void Formation in Rear Local Contacts of Silicon Solar Cells, IEEE Journal of Photovoltaics, 6 (2016) 68-73.

[46] C. Kranz, U. Baumann, B. Wolpensinger, F. Lottspeich, M. Müller, P. Palinginis, R. Brendel, T. Dullweber, Void formation in screen-printed local aluminum contacts modeled by surface energy minimization, Solar Energy Materials and Solar Cells, 158, Part 1 (2016) 11-18.

[47] E. Urrejola, K. Peter, H. Plagwitz, G. Schubert, Distribution of Silicon in the Aluminum Matrix for Rear Passivated Solar Cells, Energy Procedia, 8 (2011) 331-336.

[48] K. Dressler, M. Rauer, M. Kaloudis, S. Dauwe, A. Herguth, G. Hahn, Nondestructive Characterization of Voids in Rear Local Contacts of PERC-Type Solar Cells, IEEE Journal of Photovoltaics, 5 (2015) 70-76.

[49] S. Großer, S. Swatek, J. Pantzer, M. Turek, C. Hagendorf, Quantification of Void Defects on PERC Solar Cell Rear Contacts, Energy Procedia, 92 (2016) 37-41.

[50] B. Hallam, B. Tjahjono, T. Trupke, S. Wenham, Photoluminescence imaging for determining the spatially resolved implied open circuit voltage of silicon solar cells, Journal of Applied Physics, 115 (2014) 044901.

[51] O. Breitenstein, Nondestructive local analysis of current–voltage characteristics of solar cells by lock-in thermography, Solar Energy Materials and Solar Cells, 95 (2011) 2933-2936.

[52] R. Horbelt, G. Hahn, R. Job, B. Terheiden, Void Formation on PERC Solar Cells and Their Impact on the Electrical Cell Parameters Verified by Luminescence and Scanning Acoustic Microscope Measurements, Energy Procedia, 84 (2015) 47-55.

[53] W. Kern, HANDBOOK OF SEMICONDUCTOR WAFER

CLEANING TECHNOLOGY

Science, Technology, and Applications, Noyes Publications, 1993.

[54] E. Britannica, https://www.britannica.com/science/electromotive-series., in.

[55] D. Hellin, S.D. Gendt, J. Rip, C. Vinckier, Total reflection X-ray fluorescence spectrometry for the introduction of novel materials in clean-room production environments, IEEE Transactions on Device and Materials Reliability, 5 (2005) 639-651.

[56] Y.Y. Zhonglan LI, Xueling ZHANG, Zhiqiang FENG and Pierre J. VERLINDEN, HIGH-LIFETIME WAFER CLEANING METHOD USING OZONE DISSOLVED IN DIW/HF/HCL SOLUTION, in: 29th European Photovoltaic Solar Energy Conference and Exhibition, Amsterdam, 2014.

[57] H. Angermann, K. Wolke, C. Gottschalk, A. Moldovan, M. Roczen, J. Fittkau, M. Zimmer, J. Rentsch, Electronic interface properties of silicon substrates after ozone based wet-chemical oxidation studied by SPV measurements, Applied Surface Science, 258 (2012) 8387-8396.

[58] http://www.oxidationtech.com/ozone/ozone-production/corona-discharge.html.

[59] M. Haslinger, M. Soha, S. Robert, M. Claes, P.W. Mertens, J. John, 'Just-Clean-Enough': Optimization of Wet Chemical Cleaning Processes for Crystalline Silicon Solar Cells, Solid State Phenomena, 255 (2016) 344-347.

[60] F.D. Smedt, C. Vinckier, I. Cornelissen, S.D. Gendt, M. Heyns, A Detailed Study on the Growth of Thin Oxide Layers on Silicon Using Ozonated Solutions, Journal of The Electrochemical Society, 147 (2000) 1124-1129.

[61] M. Grundner, Hahn, P. I., Lampert, I., Schnegg, A. and Jacob, H.,, Proc. First International Symposium on Cleaning Technology in Semi- conductor Device Manufacturing, The Electrochemical Society, 90-9 (1990) 215-226.

[62] https://chem.libretexts.org/Core/Physical_and_Theoretical_Chemistry/Kinetics/Case_Studies%3A_Kinetics/Depletion_of_the_Ozone_Layer, Depletion of Ozone Layer.

[63] J. Bullock, D. Yan, A. Cuevas, B. Demaurex, A. Hessler-Wyser, S.D. Wolf, Passivated contacts to n+ and p+ silicon based on amorphous silicon and thin dielectrics, in: 2014 IEEE 40th Photovoltaic Specialist Conference (PVSC), 2014, pp. 3442-3447.

[64] F. Feldmann, M. Bivour, C. Reichel, M. Hermle, S.W. Glunz, Passivated rear contacts for high-efficiency n-type Si solar cells providing high interface passivation quality and excellent transport characteristics, Solar Energy Materials and Solar Cells, 120, Part A (2014) 270-274.

[65] J. Bullock, A. Cuevas, T. Allen, C. Battaglia, Molybdenum oxide MoOx: A versatile hole contact for silicon solar cells, Applied Physics Letters, 105 (2014) 232109.

[66] X. Yang, Q. Bi, H. Ali, K. Davis, W.V. Schoenfeld, K. Weber, High-Performance TiO2-Based Electron-Selective Contacts for Crystalline Silicon Solar Cells, Advanced Materials, 28 (2016) 5891-5897.

[67] G. Dingemans, W.M.M. Kessels, Status and prospects of Al2O3-based surface passivation schemes for silicon solar cells, Journal of Vacuum Science & Technology A: Vacuum, Surfaces, and Films, 30 (2012) 040802.

[68] N.P. Kobayashi, C.L. Donley, S.-Y. Wang, R.S. Williams, Atomic layer deposition of aluminum oxide on hydrophobic and hydrophilic surfaces, Journal of Crystal Growth, 299 (2007) 218-222.

[69] S.M. George, Atomic Layer Deposition: An Overview, Chemical Reviews, 110 (2010) 111-131.

[70] G. Dingemans, Nanolayer surface passivation schemes for silicon solar cells, in, Eindhoven University of Technology, 2011.

[71] T. Weckman, K. Laasonen, First principles study of the atomic layer deposition of alumina by TMA-H2O-process, Physical Chemistry Chemical Physics, 17 (2015) 17322-17334.

[72] Y. Yuan, T.R. Lee, Contact Angle and Wetting Properties, in: G. Bracco, B. Holst (Eds.) Surface Science Techniques, Springer Berlin Heidelberg, Berlin, Heidelberg, 2013, pp. 3-34.

[73] D.E. Kane, R.M. Swanson, Measurement of the emitter saturation current by a contactless photoconductivity decay method, in: IEEE Photovoltaic Specialists Conference, 1985.

[74] D.K. Schroder, D.L. Meier, Solar cell contact resistance—A review, IEEE Transactions on Electron Devices, 31 (1984) 637-647.

[75] L. Tous, Nickel/Copper Plated Contacts as an Alternative to Silver Screen Printing for the Front Side Metallization of Industrial High Efficiency Silicon Solar Cells, 2014.